

3D Printable Lithium Ion Batteries and the Effect of Aspect Ratio of CuAg Nanowires on
Graphite Anode Performance.

by

Christopher Reyes

Department of Chemistry
Duke University

Date: _____

Approved:

Benjamin J. Wiley, Supervisor

Jeffrey T. Glass

Aaron D. Franklin

Patrick Charbonneau

Dissertation submitted in partial fulfillment of
the requirements for the degree of Doctor
of Philosophy in the Department of
Chemistry in the Graduate School
of Duke University

2018

ABSTRACT

3D Printable Lithium Ion Batteries and the Effect of Aspect Ratio of CuAg Nanowires on
Graphite Anode Performance.

by

Christopher Reyes

Department of Chemistry
Duke University

Date: _____

Approved:

Benjamin J. Wiley, Supervisor

Jeffrey T. Glass

Aaron D. Franklin

Patrick Charbonneau

An abstract of a dissertation submitted in partial
fulfillment of the requirements for the degree
of Doctor of Philosophy in the Department of
Chemistry in the Graduate School of
Duke University
2018

Copyright by
Christopher Reyes
2018

Abstract

The majority of consumer electronic devices, electric vehicles, and aerospace electronics are powered by lithium ion batteries because of their high energy and power densities. Commercially available lithium ion batteries consist of electrodes, separators and current collectors fabricated in multilayer rolls that are packaged in cylindrical or rectangular cases. The size and shape of the package as well as the composition of the electrode has a significant impact on the battery life and design of the products they power. For example, the battery life and shape of portable electronics such as cell phones or laptops, is governed by the volume that is dedicated to the battery. In the case of electric vehicles, decreasing the size and weight of the battery while increasing capacity is an engineering challenge that affects vehicle range and cost. Therefore, the of my dissertation consists of the development of a novel 3D printable lithium ion battery nanocomposites and the integration of conductive metal nanomaterials into conventional lithium ion anodes. Here, we report the development of PLA-anode, cathode, and separator materials that enable 3D printing of complete lithium ion batteries with a low-cost FFF printer for the first time. The most common 3D printing polymer polylactic acid (PLA) is an insulator. However, our work demonstrates that 3D printed PLA can be infused with a mixture of ethyl methyl carbonate, propylene carbonate, and LiClO_4 provides an ionic conductivity of $2.3 \times 10^{-4} \text{ S cm}^{-1}$ which is comparable to that of polymer and hybrid electrolytes (10^{-3} to $10^{-4} \text{ S cm}^{-1}$). It was found that up to 12-30 volume % of solids, depending on the filler

morphology, could be mixed into PLA without causing it to clog during 3D printing. It was also found that not only is electrical conductivity crucial to the performance of a 3D printed lithium ion battery, but efficient electrical contact to the active materials is as well. To that effect, we investigated the effect of aspect ratio of silver-copper core-shell nanowires on the performance enhancement of a commercially fabricated graphite lithium ion anodes. Currently, carbon is the most common conductive filler used in commercial lithium ion battery anodes. We hypothesize that a more conductive, high aspect ratio would improve the performance of a lithium ion battery. We examined the effect of exchanging carbon with CuAg nanowires as the conductive filler in graphite lithium ion batteries. We tested 4 different aspect ratios and found that not only does aspect ratio matter, diameter and length have profound effect on capacity and energy of the anode at the same volume percent as carbon conductive filler under similar experimental conditions.

Dedication

I would like to dedicate this work to my wonderful wife Zava, for supporting me as we moved halfway across the country with a new born so that I can pursue my dreams. Also, to my two kids, Zuri and Lars, who have become my biggest motivators. Finally, I would like to dedicate this to my late mother Frances, for showing me how to persevere and be strong through the toughest of times.

Table of Contents

Abstract	iv
Dedication	vi
List of Tables	ix
List of Figures	x
1. Introduction	12
1.1 Applications and Motivations for 3D Printing Lithium Ion Batteries.....	13
1.2 Advanced Fabrication Methods for Improving the Energy Density of Lithium Ion Batteries	14
2. Lithium Ion Battery Fundamentals	16
2.1 Electronic and Ionic Conductivity in Lithium Ion Batteries	19
2.2 Electronic and Ionic Conductivity Measurements	14
3. 3D Printed Lithium Ion Batteries	23
3.1 Ionic Conductivity of Poly Lactic Acid	23
3.1.1 Infusion of Poly Lactic Acid.....	24
3.1.2 Ionic Conductivity of Infused Poly Lactic Acid	25
3.2 Printable Electrode Optimization	27
3.2.1 Solids Loading and Conductivity	28
3.2.2 Conductive Filler to Active Material Ratios	23
3.3 3D Printed Electrode Half-Cell Characterization	31
3.3.1 Preparation of 3D Printable Electrode Filaments.....	31
3.3.2 3D Printed Anode and Cathode Characterization.....	32

3.4 3D Printed Full Cell Lithium Ion Batteries.....	37
3.4.1 3D Printed Full Cell Fabrication and Characterization.....	38
3.5 Single Print, 3D Printed Lithium Ion Battery.....	40
3.5.1 Layer by Layer 3D Printed Lithium Ion Battery Characterization.....	43
3.6 3D Printed Wearable Lithium Ion Batteries	38
3.6.1 3D Printed LED Sunglasses and LED Brangle Bracelet	38
3.7 Summary	47
4. Cu-Ag Core-Shell Nanowire Conductive Filler for Lithium Ion Battery Anodes	48
4.1 Fabrication of Nanowire Conductive Filler Anode	48
4.1.1 Cu Nanowire Synthesis	49
4.1.2 Ag Coating.....	50
4.1.3 Cu-Ag Core-Shell Nanowire Characterization	52
4.2 Results for Anode Characterization	53
4.2.1 Anode Fabrication and Resistivity.....	53
4.2.2 Anode Rate Performance.....	56
4.2.3 Performance Increase and Cycling Stability	58
4.2.4 Anode Porosity and Composition.....	61
4.2.5 Effect of Aspect Ratio and Porosity on Internal Resistance.....	64
4.3 Summary	66
5. Conclusion	66
References	69
Biography.....	79

List of Tables

Table 1: Sample labeling scheme with aspect ratios, lengths and diameters of AgCu NWs used as conductive filler in each graphite anode.	53
--	----

List of Figures

Figure 1: Lithium Ion Battery Schematic.....	18
Figure 2: Conduction in a Lithium Ion Battery.....	19
Figure 3: 2-Point Probe Measurement.....	20
Figure 4: 4-Point Probe Measurements.....	21
Figure 5: ElectroImpedance Spectroscopy.....	22
Figure 6: Enhancing the Ionic Conductivity of PLA.....	25
Figure 7: Nyquist plot of Infused PLA.....	26
Figure 8: SEM Images of Conductive Carbons and Electrode Optimizations.....	28
Figure 9: SEM Images of Active Materials.....	30
Figure 10: Filament Fabrication.....	32
Figure 11: 3D Printed Half Cell Characterization.....	35
Figure 12: XPS of 3D Printed Electrodes.....	37
Figure 13: 3D Printed Coin Cell Characterization.....	39
Figure 14: Nyquist Plot for 3D Printed Half-Cells.....	40
Figure 15: 3D Printing a Single Print Battery.....	42
Figure 16: Single Print Battery.....	44
Figure 17: 3D Printed Wearables.....	46
Figure 18: Cu NW Synthesis.....	50
Figure 19: Oxidation Resistance of Cu-Ag Core-Shell Nanowire.....	51
Figure 20: CuAg NW vs Cu NW Anode Stability Comparison.....	52
Figure 21: Anode Aerial SEM Images.....	54

Figure 22: Anode Cross Sections, Aspect Ratios and Resistivities.....	56
Figure 23: Gravimetric Capacities.....	58
Figure 24: Capacity Increases	59
Figure 25: Anode Cycling Stability	61
Figure 26: CuAg Nanowire Aerogels.....	62
Figure 27: Porosity and Electrode Composition.....	63
Figure 28: Nyquist plot of Anodes	64
Figure 29: Charge Transfer and SEI Resistance	65

1. Introduction

In 1981, Dr. John B. Goodenough filed a patent for a new energy storage technology that we now know as the Lithium Ion Battery (LIB).¹ A few years later, work by Yazami *et al*, particularly in graphite as an anode material brought the lithium ion battery closer to commercialization.² It took a decade of development before the Sony Corporation commercialized and released its first generation of Lithium Ion Batteries (LIBs) for its portable electronic devices.¹ Since then, LIBs have become a ubiquitous part of our lives as they power most portable electronics, i.e. cell phones and laptops, as well as electric vehicles [EVs] because of the high volumetric and gravimetric energy densities which allow for a small size, light weight battery.³⁻⁴ However, LIBs are reaching their performance limits and demands from EVs and renewable storage are causing industry to look for new ways to enhance their performance.

In this thesis, we start in Chapter 1 by introducing the fundamentals of LIB's including components, chemistry, ionic and electronic conductivity as well as performance benchmarks and calculations. We also discuss applications and fabrication methods used in industry followed by the motivation for 3D printing LIBs. We then discuss advanced fabrication techniques and previous research that has been performed in the field. The importance of conductivity, both electronic and ionic, is explained and we then focus on current and previous work on improving the energy density of LIBs. In Chapter 2, I focus on a complete LIB fabricated using Fused Filament Fabrication (FFF),

or more commonly known as 3D printing. We highlight the development of 3D printable, polymer-based filaments and the key metrics that enable this technology. In Chapter 3, we turn our focus to conventional LIBs and concentrate on the electronic conductivity of the anode. Here, we discuss the usage of Cu-Ag core-shell nanowires as a replacement for carbon as the conductive additive in a conventional graphite LIB anode. In particular, we examine the effect of aspect ratio on several performance metrics including rate performance as well as gravimetric and volumetric capacity and energy density. Finally, we conclude with a summary of the work we have done to ultimately enhance several performance aspects of using 3D printing and nanomaterials.

1.1 Applications and Motivations for 3D Printing Lithium Ion Batteries

The majority of consumer electronic devices, electric vehicles, and aerospace electronics are powered by LIBs because of their high energy and power densities.⁵ Commercially available LIB consist of an anode, cathode, separator and current collectors fabricated in multilayer rolls that are packaged in cylindrical or rectangular cases.⁶ Commercial LIBs are fabricated in atmosphere controlled environments as moisture with an LIB can be detrimental to its performance, life span and safety. Ref The size and shape of the package has a significant impact on the battery life and design of the products they power.⁷ For example, the battery life and shape of portable electronics such as cell phones or laptops, is governed by the volume that is dedicated to the battery. In the case of electric vehicles, decreasing the size and weight of the battery while increasing capacity is an

engineering challenge that affects vehicle range and cost.³ These size and weight restrictions are critical in space applications where cost of a launch can exceed US \$10,000/kg.⁸ The need to maximize energy storage capabilities while minimizing size and weight requires the development of approaches to design and fabricate batteries that can conform to any shape and serve as a structural component.^{3,9}

1.2. Advanced Fabrication Methods for Improving the Energy Density of Lithium Ion Batteries

There has been significant recent efforts to develop batteries with unconventional shapes and structural batteries to overcome form factor limitations. Research efforts in unconventional form factors include: spray paintable batteries, thin paper batteries, printable solid-state or PRIS batteries, and stretchable wire-shaped batteries.^{7, 10-12} Other approaches include 3D printing technologies such as ink printed electrodes, fused filament fabrication (FFF) 3D printed graphene electrodes, and 3D printed ceramic-polymer electrolytes.¹³⁻²² These LIB technologies alleviate inherent form factor restrictions by creating small or thin batteries that can conform to the surface of an object.²³⁻²⁴ Structural batteries on the other hand increase the energy and power density of the entire system by serving as a multifunctional structural component.²⁵ Examples of structural batteries consist of reinforced electrode composites for use as body panels for electric vehicles and unmanned aerial vehicles.^{2, 3, 5, 7, 24, 25} Other structural battery work integrates commercially available LIBs into a cavity of a panel that is then used as a multifunctional, structural component of a space craft or satellite.²⁶⁻³⁰

Although previous work increases the energy density of the entire system by altering the form factor of the battery, most have complicated or expensive fabrication methods and are still restricted in overall freedom of design. Previous printed and multifunctional structural approaches are generally limited to curved or flat surfaces.^{13-22, 26-30} 3D printing has the ability to make complex 3D objects and change designs without having to modify the manufacturing process, which in turn can greatly accelerate prototyping and product development.³¹ Current additive manufacturing technologies use structural or conductive materials which has led to an increased interest in the field of 3D printed electronics.³²⁻³⁷ The Voxel8 , a multi-material 3D printer developed by a Lewis et al., is capable of producing functional electronic devices, such as quad copters and watches, by using a combination of FFF and conductive inks to wire circuit components imbedded in a 3D printed object.³³ Still, these 3D printed electronics must be designed around batteries, prohibiting the ability to design a product in any shape or form. To overcome this limitation, we need the ability to 3D print the battery, structural and electronic components concurrently. However, to enable rapid prototyping of custom battery form factors, all the components of the battery, including the anode, cathode, separator, current collector, and case, need to be 3D printable. To make this approach widely accessible, it would be beneficial if each part of the battery could be printed with low-cost, FFF 3D printers.

A major hurdle to creating 3D printable LIBs is that polymers typically used for FFF 3D printing, such as polylactic acid (PLA), are not ionic conductors. Typical hybrid, polymer, gel and composite electrolytes exhibit ionic conductivities ranging from 10^{-5} S cm^{-1} to 10^{-3} S cm^{-1} .³⁸⁻⁴⁴ Very little has been reported on PLA-based electrolytes. Chew et al. found that PLA can be used as a biodegradable solid polymer electrolyte by using lithium salts and oxide nanoparticles, achieving an ionic conductivity of 2×10^{-5} S cm^{-1} .⁴⁵⁻⁴⁶

2. Lithium Ion Battery Fundamentals

As ubiquitous as lithium ion batteries have become, it is important to describe its operation. A conventional LIB is comprised of a copper current collector, anode, separator, cathode, aluminum current collector and a case which is filled with electrolyte.

⁶ Each electrode, anode or cathode, is comprised of an active material for lithium storage, a conductive carbon to enhance electron transport and a polymer binder. The active materials for commercial lithium ion batteries is typically graphite for the negative anode and Lithium Cobalt Oxide [LCO] for the positive cathode. The separator is typically a porous polymer 25 μm soaked in electrolyte whose purpose is to electrically isolate the anode from the cathode to prevent shorting. The electrolyte is a 1 M solution of a lithium salt in a carbonate solvent. During charging, electrons from an external power source travel from the current collector, thru the conductive carbon to the graphite where they reduce the lithium ions.⁴⁷ During charging, the lithium ions are intercalating between the sheets of the graphite particle where they are stored in a 6:1 Carbon: Lithium ratio.⁴⁸⁻⁵⁰

During discharge, a resistive load - cell phone, laptop, car - is connected to the battery where the lithium in the graphite is oxidized and the electrons flow thru the device to the cathode.⁵¹⁻⁵² In the cathode, lithium ions travel thru the separator and are once again reduced and inserted in the active material. A schematic of the charge discharge process of a lithium ion battery can be seen below in Figure 1. The method of lithium storage within the active material can be categorized in to three groups; intercalation and insertion, alloying and conversion.⁵³ Intercalation and insertion have just been described in the explanation of the charge-discharge process of a graphite – LCO battery and this process is focused in this thesis. It is, however, worth briefly discussing the other two lithium storage methods as they pose to greatly increase the lithium storage capabilities of lithium ion batteries. Alloying materials store lithium by alloying lithium metal atoms with Group IV elements such as silicon, which can store 10x more lithium per gram of material.⁵³⁻⁵⁶ In conversion electrodes, a transition metal compound MX where M is a metal and X is typically P, S, O, F or Cl.⁵³ During the electrochemical reaction, the metal ion is reduced and replaced with lithium ion.^{52, 57}

How Lithium-Ion Batteries Work

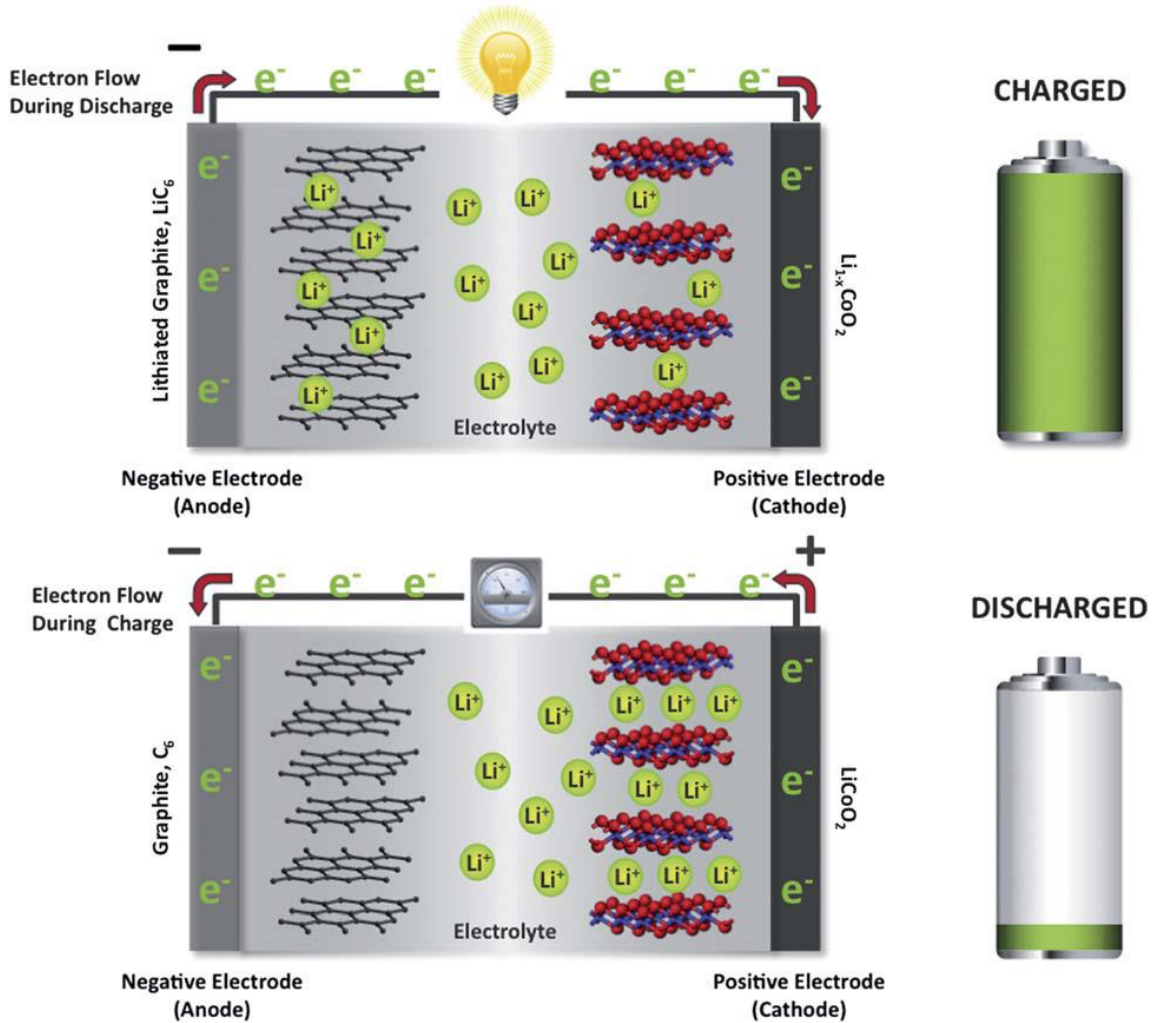


Figure 1. Lithium Ion Battery Schematic. Charge-Discharge process for a graphite anode, LCO cathode lithium ion battery.⁴⁷ This schematic is typical of a commercially available lithium ion battery used in today's electronic devices.

3.1 Electronic and Ionic Conductivity in Lithium Ion Batteries

As mentioned before, in order for a lithium ion battery to work, both electrons and ions need to travel thru the battery. Electrons need to travel from the external power source or load, thru the current collector, to the conductive carbon to the active material where the redox reaction occurs.⁴⁷ Electronic conductivity is effected by the electrical conductivity of the active material and conductive material and the contact resistance between the active material, conductive material and the current collector.⁴⁵ The lithium ion, on the other hand, need to travel from the active material in an electrode, thru the separator, to the counter electrode.⁵⁸⁻⁶⁰ The Figure 2 below depicts the pathways of an electron and ion in a typical LIB system.

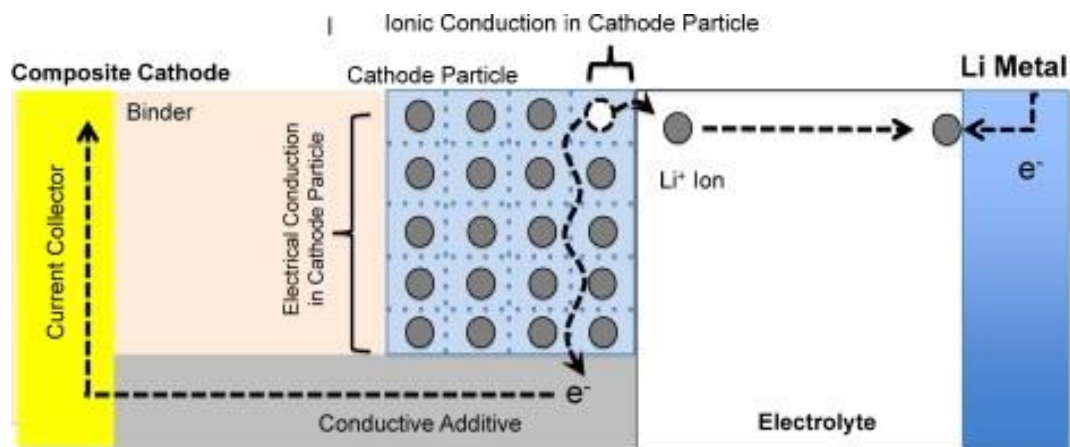


Figure 2. Conduction in a Lithium Ion Battery. Conduction pathways of electrons and lithium ions in a lithium ion battery cell.⁴⁵

3.2 Electronic and Ionic Conductivity Measurements

To characterize the redox reaction of a LIB, we need to be able to characterize the electronic and ionic conductivities accurately. In this chapter, we will discuss the methods used in the presented works. For electrical measurements, Ohms Law, $V=I \cdot R$ is the basis for all measurements and calculations. We begin with a simple 2-Point probe resistance measurement that can be used to calculate the resistivity of a sample of known dimensions. Figure 3 below depicts the geometry and measurement points for determining resistivity.

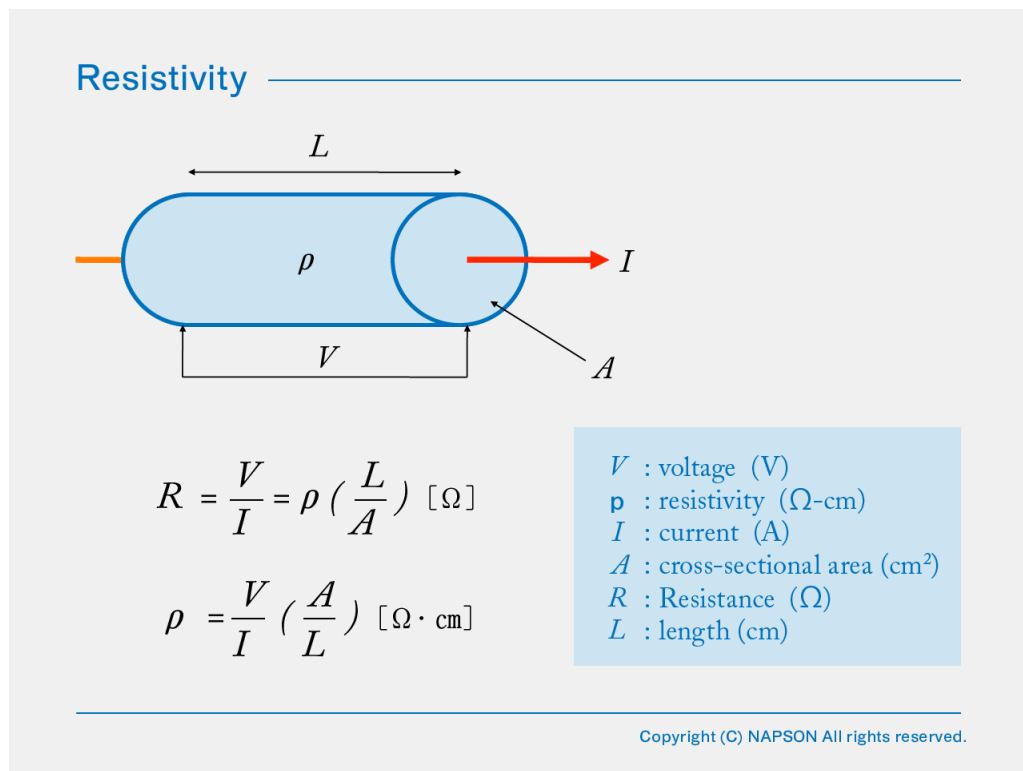


Figure 3. 2-Point Probe Measurement. Resistivity as determined by 2-Point Probe measurement. Here, the measuring probes are separated by distance L .⁶¹

For a more accurate determination of sheet resistance and resistivity, 4-Point Probe can be used in place of the 2-Point Probe. In this method, 4 equally spaced and sized probes are positioned in a straight line and a constant current is applied to the outer probes while the voltage difference is measured between the inner two probes as shown with calculations in Figure 4 below. ⁶¹

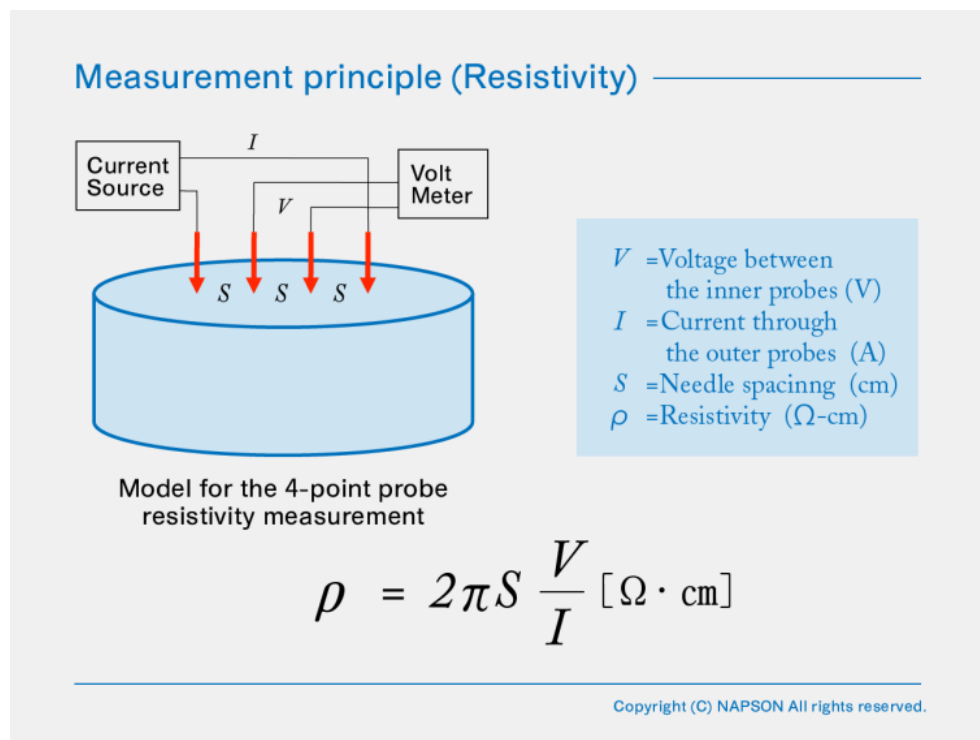


Figure 4. 4-Point Probe Measurements. Resistivity as determined by 4-Point Probe measurement. Here, the measuring probes are separated by distance S.⁶¹

For ionic conductivity, electroimpedance spectroscopy [EIS] is used to probe the motion of the ions within a sample. In this method, an alternating voltage is applied to a sample and the resulting current is measured.⁶² Ohms Law for Alternating Current [AC] circuits are employed since this method produces both real and imaginary impedances.

Here, the frequency of the applied voltage is swept from high to low frequencies, the frequency range and peak to peak [Vpp] is determined by the type of system to be measured.⁶³ The high frequency region is associated with charge transfer kinetics while the lower frequency region is associated with mass transfer kinetics.⁶⁴⁻⁶⁵ Each region is differentiated by specific shapes that appear in the real vs imaginary impedance plot, also commonly referred to as a Nyquist Plot as can be seen in the Figure 5 below.⁶²

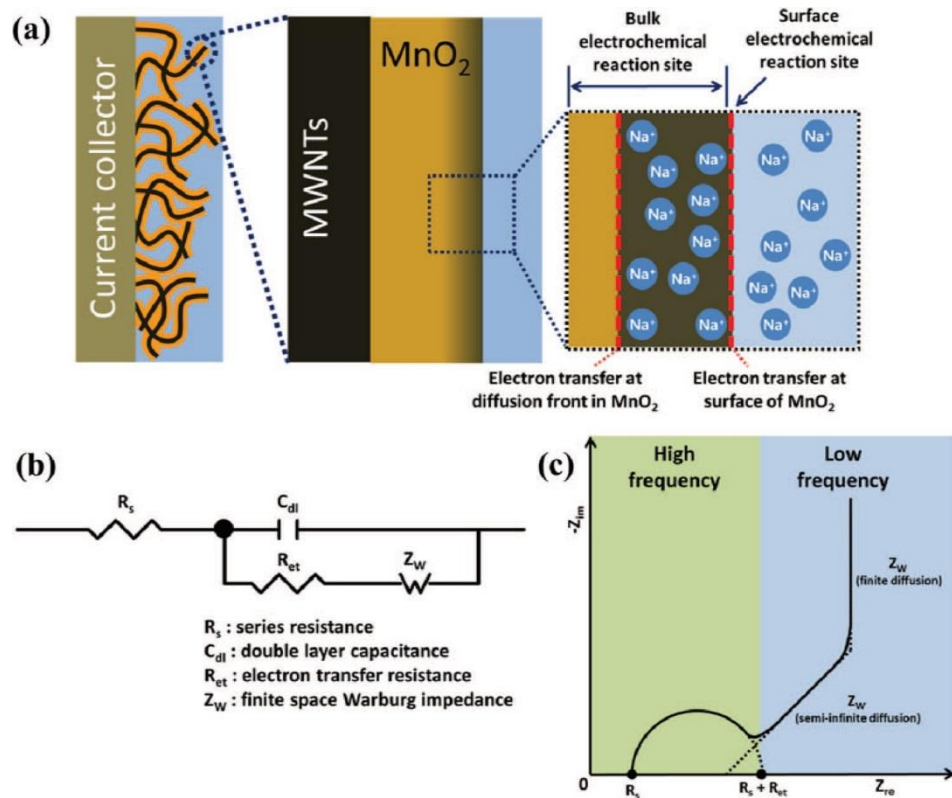


Figure 5. ElectroImpedance Spectroscopy. A) Surface and bulk electrochemical reactions being probed using EIS. B) Equivalent circuit used to model system. C) Nyquist plot of system using EIS.⁶²

3. 3D Printed Lithium Ion Batteries

Here, we report the development of PLA-anode, cathode, and separator materials that enable 3D printing of complete lithium ion batteries with a low-cost FFF printer for the first time. We further report how the amounts of conductive (Super P, graphene, multiwall-carbon nanotubes) and active (lithium titanate, lithium manganese oxide) materials in PLA composites affected their printability, as well as the performance of 3D printed batteries made from these composites. 3D printed anode and cathode electrodes were stable for 50 cycles and exhibited a capacity of $\sim 1.0 \text{ mA h g}^{-1}$ calculated using active mass in the printed anode and cathode. 3D printed full-cells were stable for 100 cycles and exhibited a capacity of 0.5 mA h g^{-1} also calculated using active mass in the printed anode and cathode. While the specific capacities of the electrodes are very low relative to their theoretical capacities, this study demonstrates the ability of the electrodes to be printed using a FFF 3D printer. We also demonstrate the possibility of creating a full 3D printed LIB in a single print with no assembly required. We show the 3D printed batteries can be used to power electronic devices such as LCD sunglasses and a LED bangle.

3.1 Ionic Conductivity of Poly Lactic Acid

We hypothesized that PLA could be converted into an ionically conducting matrix by swelling the polymer with liquid electrolytes, thereby enabling the 3D printing of a lithium ion battery. By testing 9 combinations of carbonate solvents and 3 electrolytes typically used in commercial lithium ion batteries, we determined that the ionic

conductivity of PLA can be increased up to $4.67 \times 10^{-4} \text{ S cm}^{-1}$, ~20 times higher than previous reports.⁴¹⁻⁴²

3.1.1 Infusion of Poly Lactic Acid

We measured the ionic conductivity of pure PLA to be $8.2 \times 10^{-14} \text{ S cm}^{-1}$, in agreement with previously reported values.⁴⁵⁻⁴⁶ Since the structure of the pure polymer has no ions, the measured ionic conductivity is likely due to either trace H₂O within the polymer or some ionic impurities present. Since ionic conductivities on the order of 10^{-4} to $10^{-3} \text{ S cm}^{-1}$ are required for practical devices, to improve the ionic conductivity of PLA we chose an approach of printing pure PLA and then infusing the printed polymer with an electrolyte solution to create a hybrid polymer electrolyte. Various carbonate combinations were tested to determine which would allow for the most electrolyte uptake while retaining structural integrity. Lithium ions diffuse faster through liquids than solids, so we hypothesized that greater electrolyte uptake would correlate with higher ionic conductivity.^{32-37, 45-46} Electrolyte uptake was determined by comparing changes in volume before and after PLA-solvent infusion. Electrochemical impedance spectroscopy (EIS) was used to measure the ionic conductivity and the results are plotted against the change in volume after infusion (Fig. 6a). Although diethyl carbonate (DEC) had the greatest volume increase (34%), this composite is brittle and has one of the lowest ionic conductivities. A combination of propylene carbonate (PC) and ethyl methyl carbonate (EMC) had the second highest volume change (29%) in PLA and had the highest ionic

conductivity ($6.75 \times 10^{-5} \text{ S cm}^{-1}$) (Fig 6a). Negative values of percent volume change are the result of the polymer dissolving. PC and EMC were used as the carbonate solvents for all lithium salt solutions in this report.

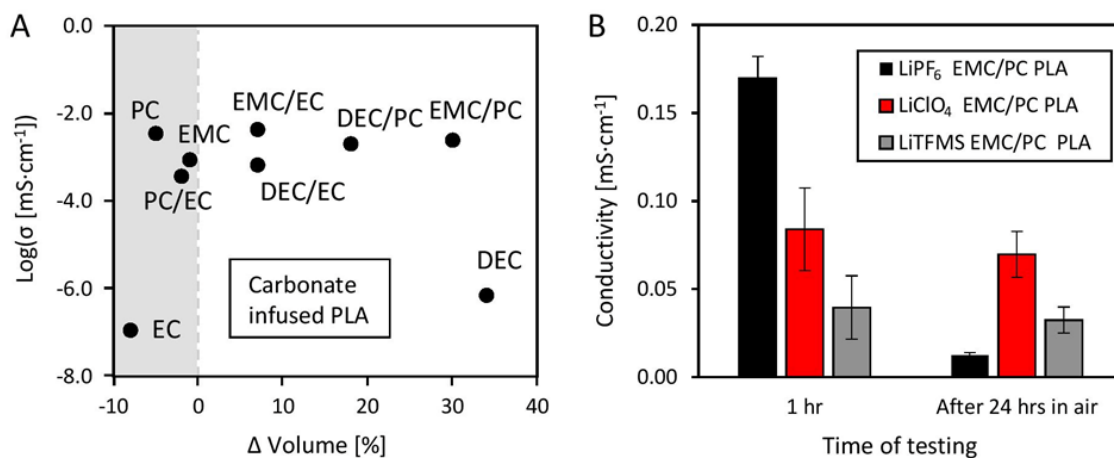


Figure 6. Enhancing the Ionic Conductivity of PLA. (A) Log ionic conductivity versus percent volume change for PLA infused with various carbonate solvents. (B) Ionic conductivity of PLA infused with lithium salts after storage in air.

3.1.2 Ionic Conductivity of Infused Poly Lactic Acid

PLA disks were printed and infused with solutions of 1 M lithium hexafluorophosphate (LiPF₆), lithium perchlorate (LiClO₄) or lithium trifluoromethanesulfonate (LiTFMS) in PC/EMC. Each sample was tested twice; once 1 hour after infusion, and again after storage on the lab bench open to air for 24 hours (Figure 6b above). The ionic conductivity for infused PLA was investigated with EIS and calculated using the following equation, $\sigma = l / (AR_b)$, where l is the thickness of the sample, A is the cross-sectional area and R_b is the bulk resistance which is extracted from a Nyquist plot.⁴¹⁻⁴² The Nyquist plot for PLA infused with 1M LiClO₄ in 50/50 vol EMC/PLA is shown in Figure 7 below.

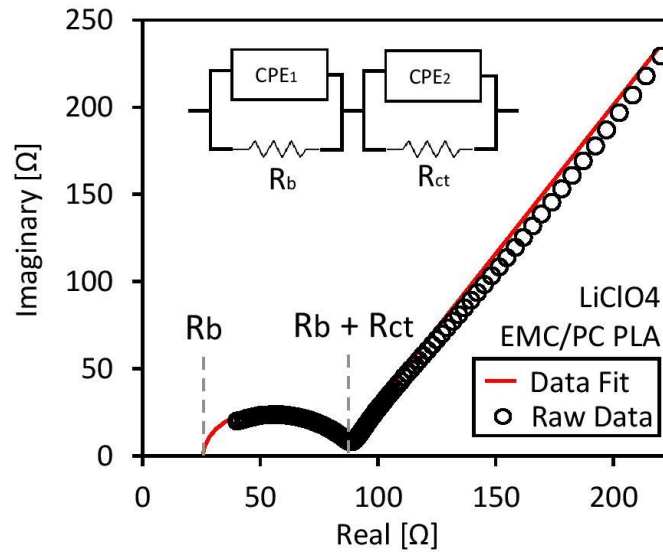


Figure 7. Nyquist plot of Infused PLA. PLA infused with 1M LiClO₄ in EMC/PC, 50/50 vol%, with equivalent circuit shown in inset.

The plot displays a charge transfer semicircle at high frequencies and a linear mass transfer region at lower frequencies.^{42, 66-67} The equivalent circuit (Figure 6b inset) used to fit EIS data is an RC circuit. The left part of the circuit consists of a constant phase element (CPE₁) in parallel with a resistive element (R_b), which represent the bulk capacitance and resistance, respectively. The right part of the circuit consists of a another constant phase element (CPE₂) in parallel with a resistive element (R_{ct}) to represent the double layer capacitance and charge transfer resistance, respectively.⁶⁷

The highest conductivity (1.7 mS·cm⁻¹, 20° C) was obtained for PLA infused with LiPF₆, but this electrolyte was not used in the final batteries because of its tendency to degrade upon exposure to moisture, causing it to lose ionic conductivity after 24 hours.⁴⁴⁻⁴⁵ Such sensitivity is not desirable for the production of 3D printing filament with reproducible

and stable ionic conductivity. PLA infused with LiClO₄ had the second highest ionic conductivity (0.085 mS·cm⁻¹, 20° C) and retained its mechanical integrity and ionic conductivity after 24 hours of exposure to ambient conditions. LiTMFS had the lowest ionic conductivity (0.039 mS·cm⁻¹, 20° C). The ionic conductivity of the LiClO₄-infused-PLA is comparable to previously reported hybrid and polymer electrolytes utilizing LiClO₄ (0.01 mS·cm⁻¹ to 1.0 mS·cm⁻¹), enabling it to be used as a printed hybrid electrolyte in a LIB.³⁶⁻³⁹

3.2 Printable Electrode Optimization

The anode and cathode need to have a high electrical conductivity in addition to a high ionic conductivity, so we next determined the maximum amount of conductive filler that could be added to the filament.⁴⁵ The total volume percent of active, conductive, and binder materials in a typical LIB electrode range from 70-90%, 5-10%, and 5-15%, respectively. However, if high volumes of solid fillers are loaded into PLA filament, the nozzle tends to clog during printing, or the filament becomes too brittle to print. In the following section we investigate the optimization of loading while maintaining 3D printability.

3.2.1 Solids Loading and Conductivity

To determine the optimal loading of filler, we prepared samples containing up to 40% of Super P, graphene and multi-walled carbon nanotubes (MWNT) (Figure 8a, b, and c below). We tested these conductive fillers because they are among the most conductive

and commonly used fillers in LIB electrodes.⁶⁸⁻⁷¹ These conductive fillers were mixed with solutions of PLA dissolved in dichloromethane. The solutions were then dried, pelletized, and extruded to create conductive filament with a diameter of 1.75 mm and approximately 40-50 cm in length.

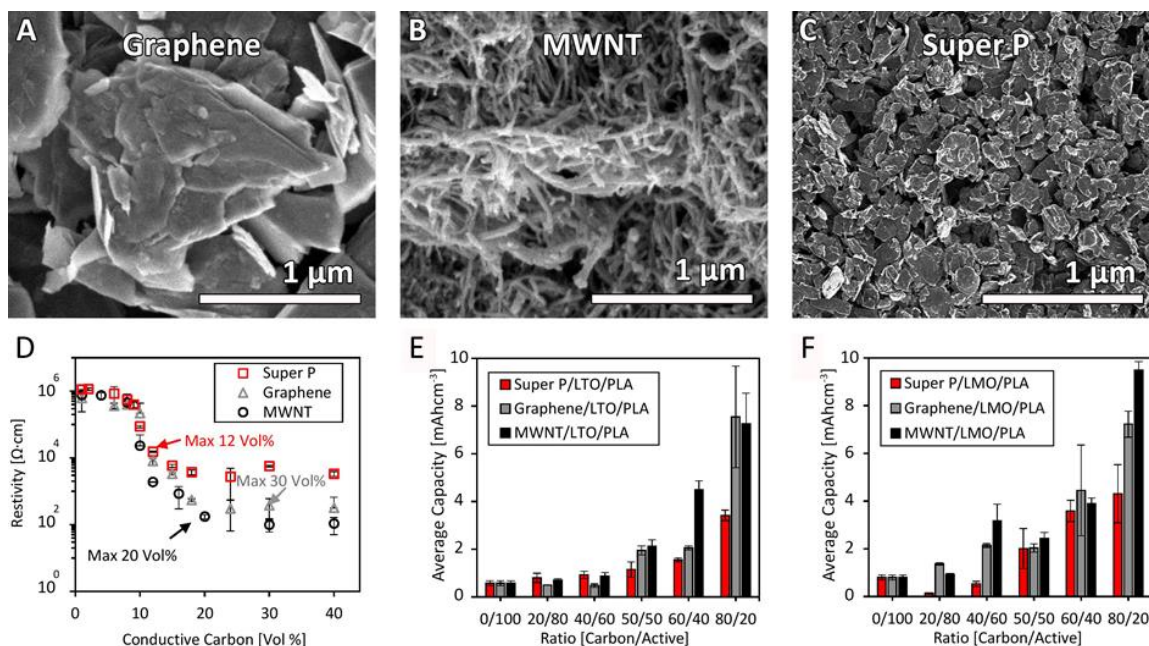


Figure 8. SEM Images of Conductive Carbons and Electrode Optimizations. (A) graphene, (B) multiwalled carbon nanotubes, (C) Super P. (D) The resistivity versus volume percent of Super P, graphene and MWNTs loaded into PLA. The maximum volume % that was also printable is labeled for each material. (E & F) Average capacity versus ratio of conductive carbon to active material in PLA for the anode and cathode, respectively.

Figure 8d shows the resistivity of these filaments as a function of volume % of the conductive filler. The filament was determined to be not printable if the filament clogged during printing of 15-25 cm of filament through a 0.4 mm nozzle, or if the filament was too brittle to load into the FFF 3D printer. The maximum volume % of conductive filler that could be loaded into the filament without degrading printability is also noted in

Figure 8d. The graphene composite had the highest printable volume loading (30%), followed by MWNTs (20%) and Super P (12%). The graphene composite began to clog during printing at volume loadings above 30% while the MWNT composite became brittle as well as clogged during printing at volume loadings above 20%. The Super P composite did not clog but became too brittle to handle at volume loadings above 12%. It is at present not clear what was the reason for the different volume percent limits for the different conductive fillers.

3.2.2 Conductive Filler to Active Material Ratios

After determining the maximum amount of filler that could be loaded into the filaments without degrading printability, we studied what ratio of active material to conductive filler resulted in the maximum energy capacity (Figure 8e and f above). The total volume percent of filler was held constant for samples containing Super P (12%), Graphene (30%) and MWNT (20%). Lithium titanate (LTO) particles 100 nm in diameter and lithium manganese oxide (LMO) particles 500 nm were added into the anode and cathode material, respectively (see Figure 9a and b for SEM images).

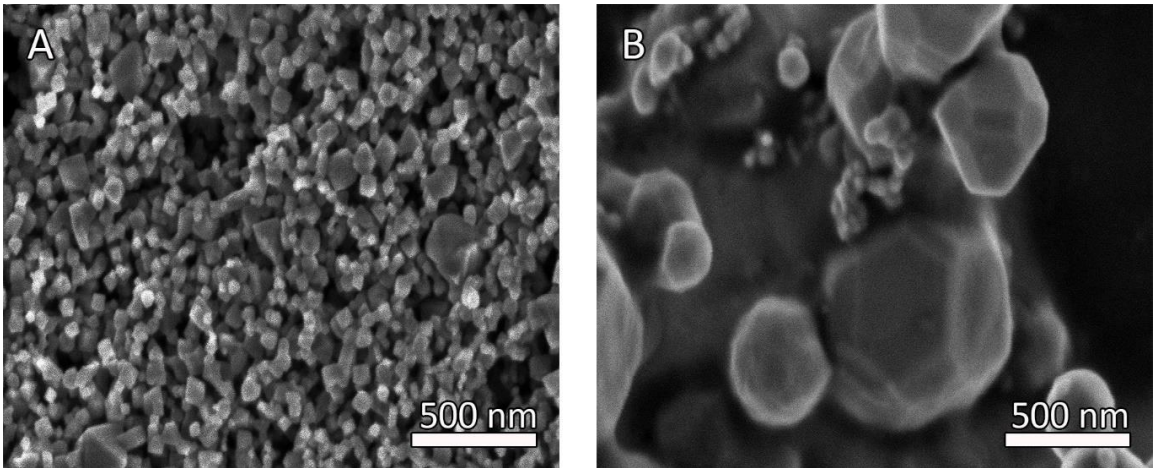


Figure 9. SEM Images of Active Materials. (A) lithium titanate (LTO) and (B) lithium manganese oxide (LMO) particles used as the active materials in the 3D printable battery.

Active anode and cathode nanomaterials were mixed into PLA at different ratios to determine the effect of carbon material type and ratio on their capacity for energy storage. LTO was chosen for the anode because of its excellent thermal stability, long cycling life span, low volume expansion and high volumetric capacity. LMO was chosen for the cathode because it has good thermal stability, low volume expansion and has a high-power density when paired with LTO.^{8,72-74} Anode and cathodes disk electrodes were 3D printed to be 150- μm -thick and 14 mm in diameter. After printing, the disks were infused with 1M LiClO_4 in 50/50 vol EMC/PC and aged prior to cycling. Specific capacity measurements were performed in a coin cell using lithium metal as the counter electrode, a 25 μm polypropylene disk as the separator, and 1M LiClO_4 in 50/50 vol PC/EMC as the electrolyte.

3.3 3D Printed Electrode Half-Cell Characterization

After maximizing the amount of filler in the polymer and optimizing the ratio of active to conductive material, large scale batches of 3D printable electrode filaments were fabricated. This allowed us to further optimize print conditions as well as print multiple batches of anode and cathode samples for further characterization.

3.3.1 Preparation of 3D Printable Electrode Filaments

Poly(lactic acid) (PLA) pellets were dried in an oven at 85 °C for at least 4 hours prior to use in order to remove moisture. PLA was dissolved in dichloromethane (DCM) (Sigma Aldrich) at 0.1 g/mL under vigorous stirring until completely dissolved. Active and conductive materials were then added, and the mixture was stirred vigorously for at least 12 hours. The solution was then cast into a Teflon lined sheet and set in a fume hood at room temperature overnight to evaporate remaining solvent. The cured composite sheets were then pelletized and dried in an oven at 85° C. A polymer extruder (Filabot.com) was used for the extrusion of 1.75 mm composite filaments. The extruder was loaded with at least 25 g of dried anode or cathode pellets and preheated to 180° C for 15 minutes. After preheating, the extruder motor was turned on to begin extrusion. Once the composite began to extrude, the temperature was lowered to 160C for the remaining extrusion time. After extrusion, the filament was stored in sealed plastic bags with desiccant to keep the PLA dry. Figure 10 below depicts the fabrication process described in this section.

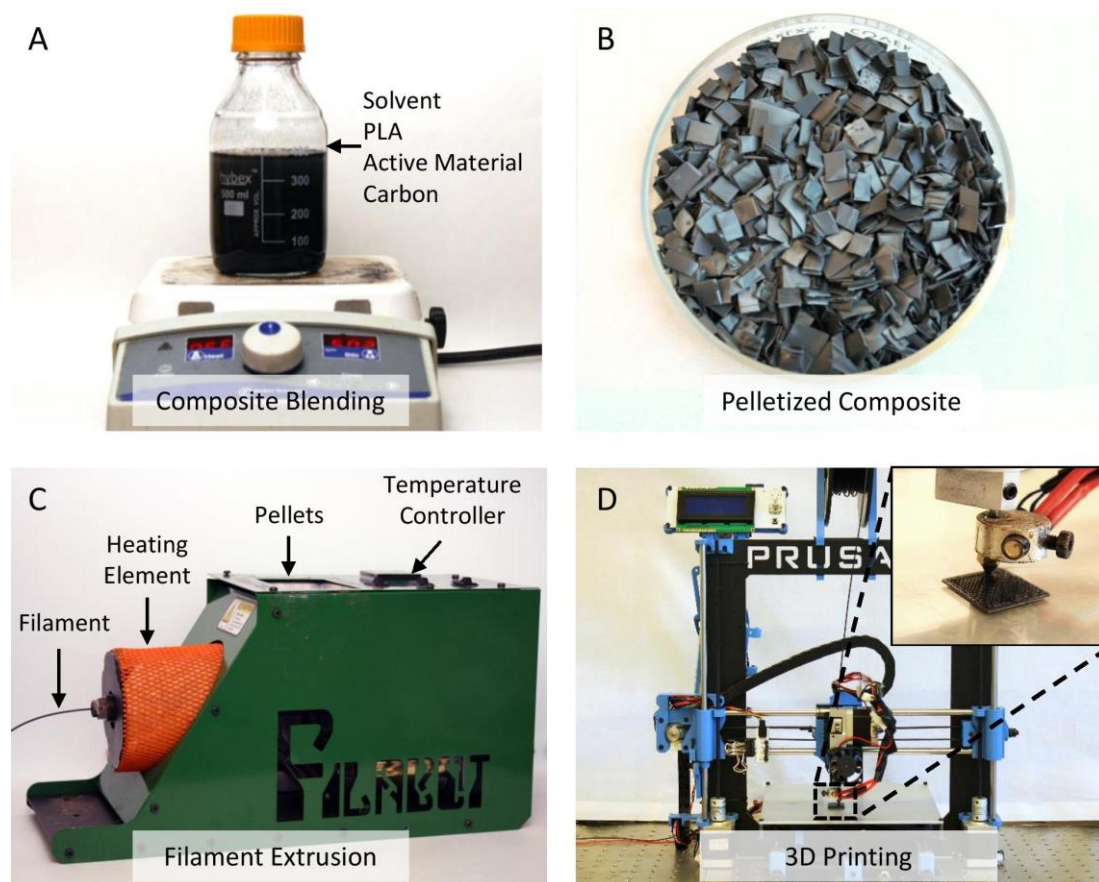


Figure 10. Filament Fabrication. (A) Image of battery composite suspension in which PLA was dissolved and blended with fillers. (B) The suspension was cast, dried and cut into pellets in preparation for extrusion. (C) The pellets are to produce a 3D printable filament 1.75 mm in diameter. (D) Electrode samples were printed using a Prusa 3D printer.

3.3.2 3D Printed Anode and Cathode Characterization

After maximizing the amount of filler in the polymer and optimizing the ratio of active to conductive material, approximately 3.0 meters of anode and cathode filament was extruded. The final composition for each electrode was 6/24/70 vol% LTO/Graphene/PLA and 4/16/80 vol% LMO/MWNT/PLA. Specific capacity calculations utilized the volume

percent of active materials (4% for LMO cathode and 6% for LTO anode). PLA was stable in both anodic and cathodic conditions as each printed half-cell was capable of at least 100 charge-discharge cycles. The printed LTO anode had a charge and discharge capacity of 4.84 mAhcm⁻³ and 3.34 mAhcm⁻³, respectively, when averaged over 100 cycles (Figure 11a). The printed LMO cathode had a charge and discharge capacity of 8.1 mAhcm⁻³ and 6.99 mAhcm⁻³, respectively, when averaged over 100 cycles (Figure 11b). The average discharge capacity for the entire printed anode and cathode (including polymer and conductive filler) is 0.34 mAhcm⁻³ and 0.71 mAhcm⁻³ respectively. The electrodes were discharged at different current densities to investigate the effect of discharge rate on capacity and capacity recovery (Figure 11 c, d). The printed LTO anode had a significant drop in capacity (from 3.81 mAhcm⁻³ to 1.10 mAhcm⁻³) when the current density was increased from 20 to 30 mA_g⁻¹. The capacity recovered to 4.46 mAhcm⁻³ when the current density was decreased to 10 mA_g⁻¹. The printed LMO cathode experienced similar capacity effects as the printed LTO anode except for a decrease in capacity (17.08 mAhcm⁻³ to 11.92 mAhcm⁻³) during the first 10 cycles at 10 mA_g⁻¹. The cathode stabilized and recovered to 13.97 mAhcm⁻³ during the last 10 cycles at 10 mA_g⁻¹. This stabilization may be due to the formation of the SEI layer and stabilization by the last set of cycling.⁷⁵ Discharge voltage curves for current densities of 10, 20, 30, and 40 mA_g⁻¹ reveal significant potential drops for the printed LTO anode (3.0-2.0V) and the printed LMO cathode (4.0-

3.3V). This large potential drop is possibly due to low conductivity and polarization caused by the polymer.⁴⁵

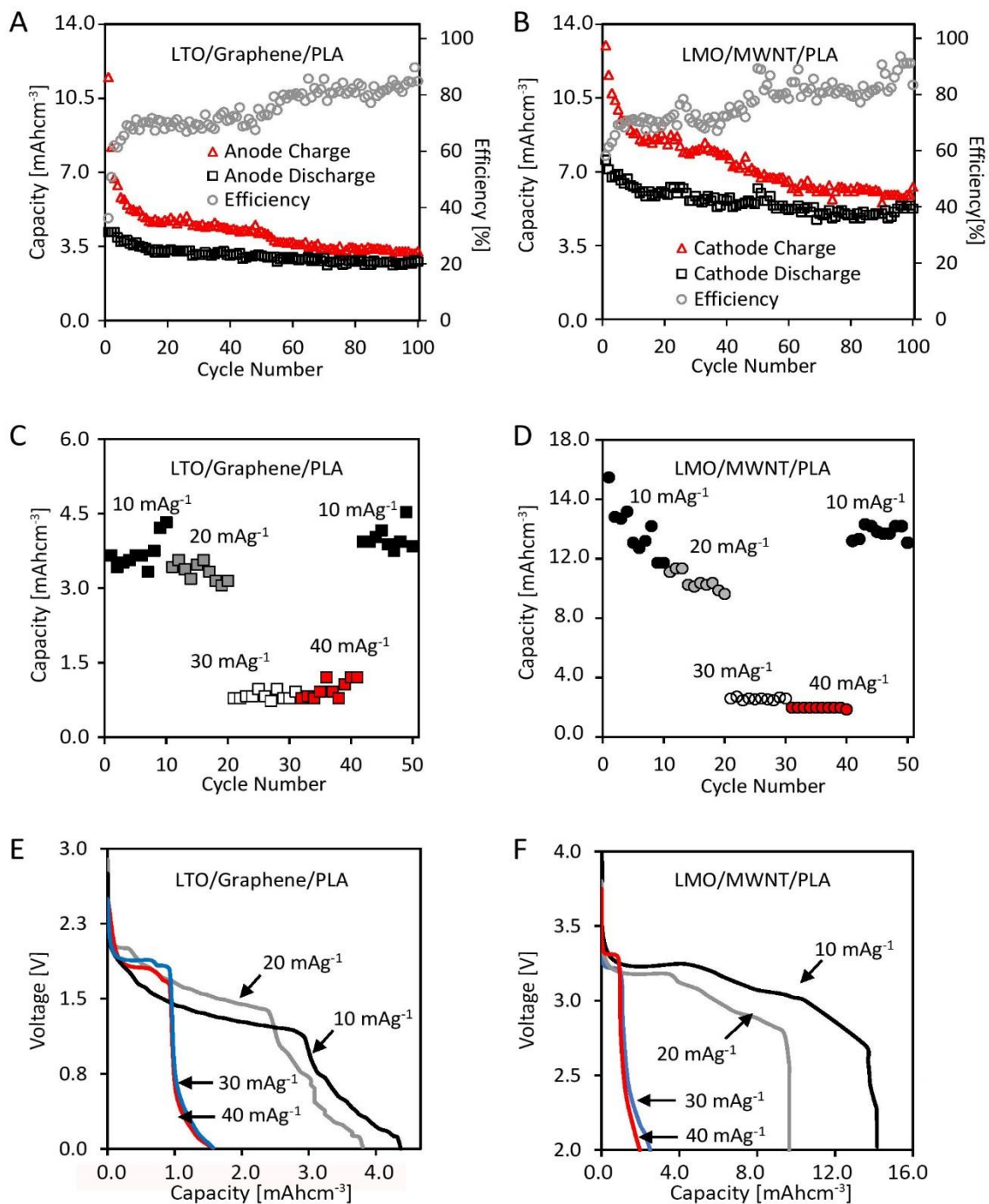


Figure 11. 3D Printed Half Cell Characterization. Anode and cathode composites testing; charge/discharge capacity and columbic efficiency of (A) anode and (B) cathode composites at a current density of 20 mAg⁻¹ for 100 cycles. (C&D) Rate performance and (E&F) discharge voltage curves of anode and cathode composites.

Both samples experienced significant capacity loss during the first 10 cycles; 50 % and 25% loss for anode and cathode, respectively. This loss is most likely due to the formation of the solid electrolyte interphase (SEI).^{45, 76-78} Evidence of SEI formation can be seen in the XPS data taken before and after cycling Figure 11 below. Pristine anode and cathodes exhibit three distinct peaks for C=O, C-O and CH in the 294-278 eV region which are associated with PLA (Figure 12 A and B).⁷⁹⁻⁸¹ This is due to the composite consisting of 70-80% polymer by volume. After cycling, both electrodes give spectra consistent with an SEI layer with peaks for LiCO_3 , Li_2C_2 , ROCO_2Li , and ROLi (Figure 12 C and D).^{49, 75, 82-84}

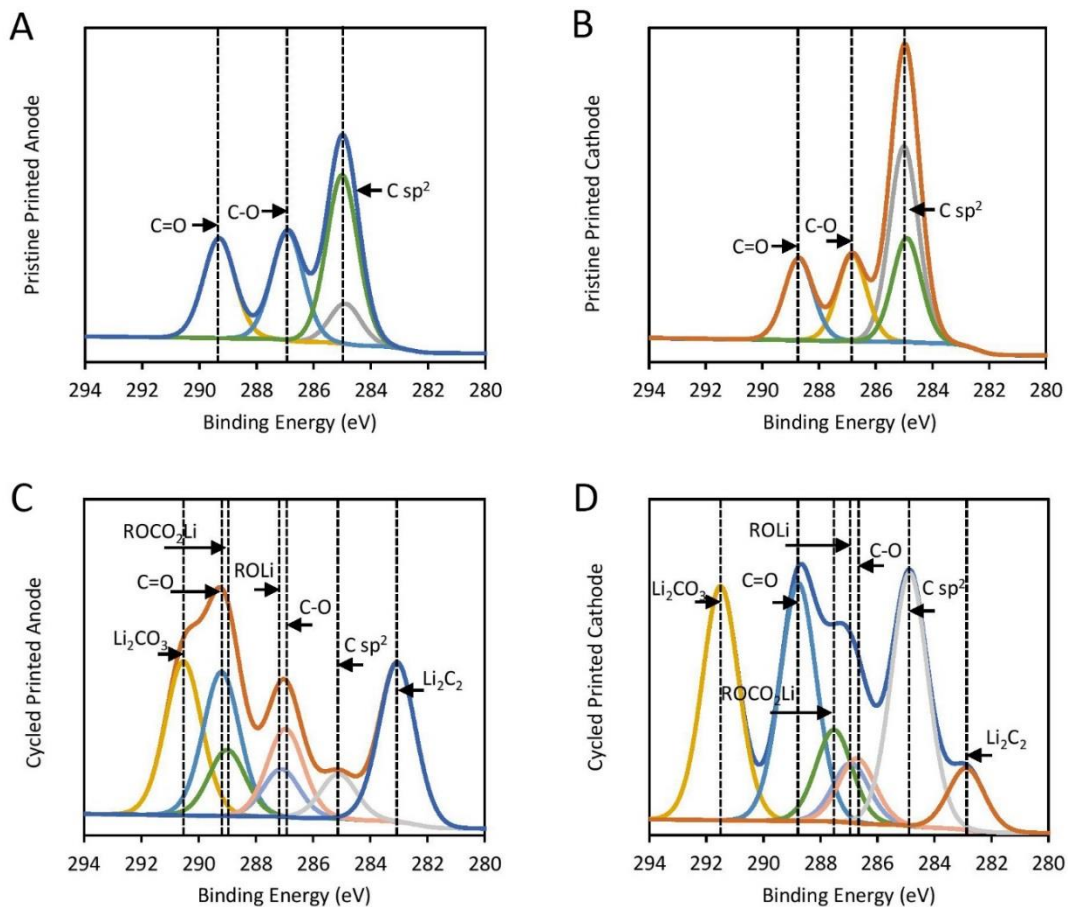


Figure 12. XPS of 3D Printed Electrodes. (A and B) XPS data for pristine 3D printed anode and cathode respectively. (C and D) XPS data for 3D printed anode and cathode after cycling.

3.4 3D Printed Full Cell Lithium Ion Batteries

Following the electrochemical characterization of the anode and cathode composite, a 3D printed full cell was tested. Printed current collectors, anode, cathode, and separator were encased in a printed coin cell (Figure 13a and b below). All printed anodes, cathodes and separators were 16 mm in diameter, 150- μm -thick, and were infused with 1M LiClO_4 in 50/50 vol EMC/PLA prior to assembly. Electrifi filament was used for 3D printing the current collectors, as it has the highest conductivity of all commercially available conductive filaments. Pure PLA was used for printing the separators.

3.4.1 3D Printed Full Cell Fabrication and Characterization

The electrochemical performance for full cells was performed within a cutoff voltage range of 3.0-2.0 V at a mass-normalized current of 20 mA g^{-1} (Figure 8c below). For comparison with the half-cell results, the full cell capacity was normalized to the active mass of the anode material. The full cell experienced large irreversible capacity loss during the first 10 cycles (22.96 mAh cm^{-3} to 9.4 mAh cm^{-3}) due to SEI formation which stabilizes near the 50th cycle (9.4 mAh cm^{-3} to 5.32 mAh cm^{-3}). This fully printed cell reached an average discharge capacity of 3.91 mAh cm^{-3} and maintained an average columbic efficiency over 88.5% after the first 50 cycles. Electrochemical stabilization of the full cell

is reflected in the improvement of the discharge plateau as it broadens from the 1st to the 100th cycle (Figure 13d below).

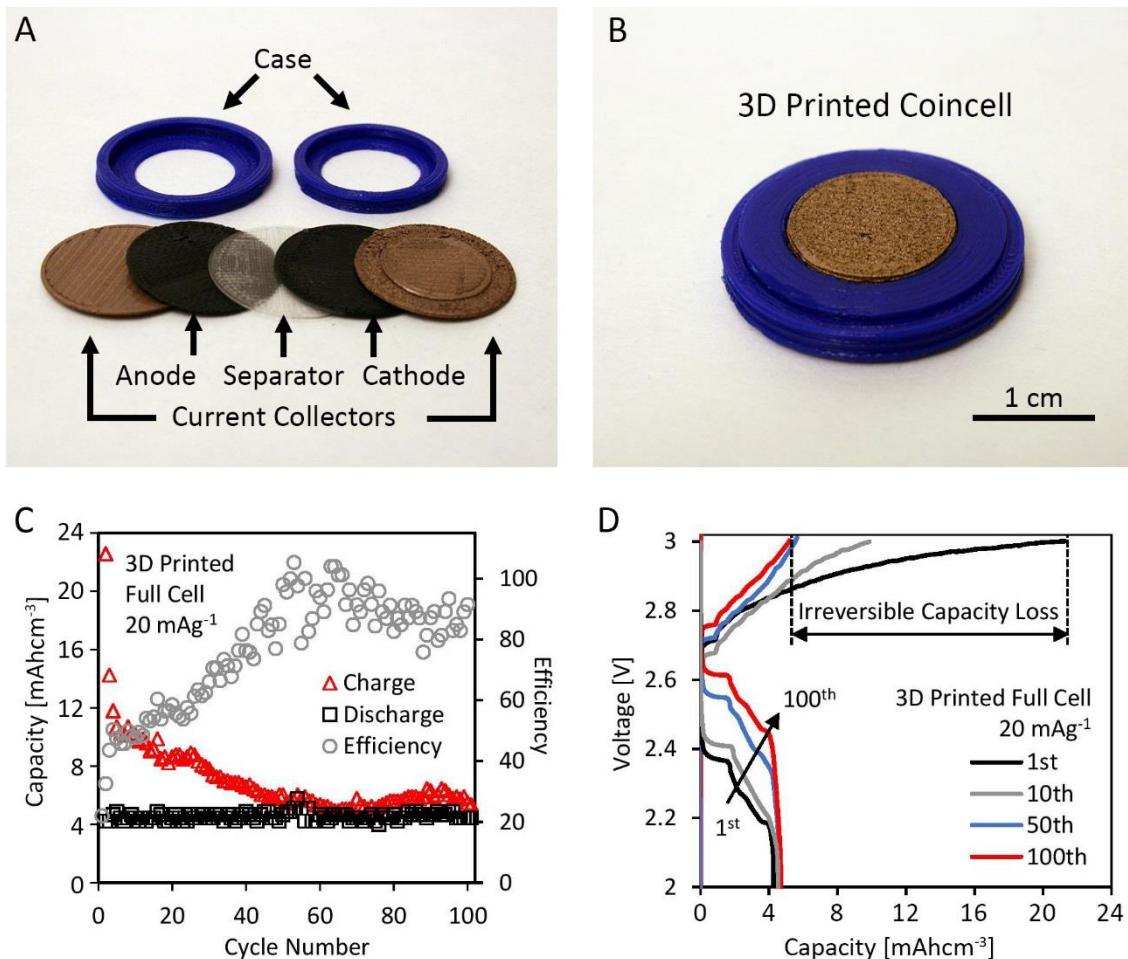


Figure 13. 3D Printed Coin Cell Characterization. (A) Individual components of the 3D printed coin cell. (B) Assembled 3D printed coin cell. (C) Capacity and columbic efficiency at a current density of 20 mA_g⁻¹ for 100 cycles. (D) Charge-discharge voltage curves for the full cell with 1st, 10th, 50th and 100th cycle shown.

It is possible that the ionic conductivity of the electrode layers may gradually increase during cycling due to increased infusion time. The capacity of the full cell (3.91 mAhcm⁻³) is less than the half cells (LTO anode 6.76 mAhcm⁻³, LMO cathode 6.99

mAhcm⁻³) possibly due to increased cell resistance created by contact resistances between printed components. Resistivity values extracted from EIS measurements (Figure 14 below) showed the use of two printed current collectors increased the resistivity from 102 Ω·cm for the half cells to 104 Ω·cm for the printed full cell. The volumetric capacity of the entire 3D printed coin cell – case, electrodes, current collectors and separator – was 0.25 mAhcm⁻³.

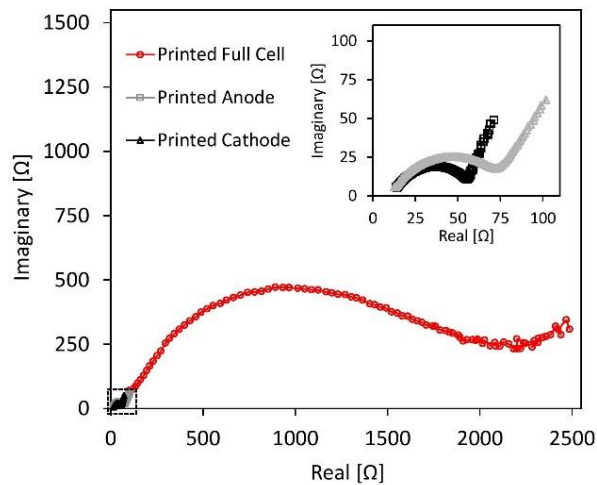


Figure 14. Nyquist Plot for 3D Printed Half-Cells. Anode and cathode half-cells and 3D printed full cell. Inset shows zoomed in region for the 3D printed anode and cathode. All EIS scans were performed at 100 mVpp from 1 MHz to 100 Hz.

3.5 Single Print, 3D Printed Lithium Ion Battery

To create a completely printed electronic device with an integrated battery and no assembly required, we need a printer with the ability to print the current collectors, anode and cathode, separator and case. Flowers and coworkers recently demonstrated the ability to create 3D printed electronics and circuits in one print using dual material FFF.⁸⁵ If this

approach could be applied to four materials, fully-printed LIB's could be integrated into electronic devices with FFF, but we lacked such a printer. To circumvent this limitation, we utilized a printing method in which the filament is exchanged during printing, enabling the 3D printing of a LIB in a single print (Figure 15 below).

A 3D model of the battery was designed with 123D (Autodesk 2016), exported as an STL file, and sliced using Cura (Ultimaker). The parameters for printing were 100 μm layer height, 50°C bed temperature, 210°C extruder temperature and 40 mm/s print speed for the cathode current collector, cathode, separator channel, and anode. A 160°C extruder temperature and 20 mm/s print speed was used for the for the anode current collector. The GCODE file was also set to pause after printing each component layer so that the filament could be exchanged.

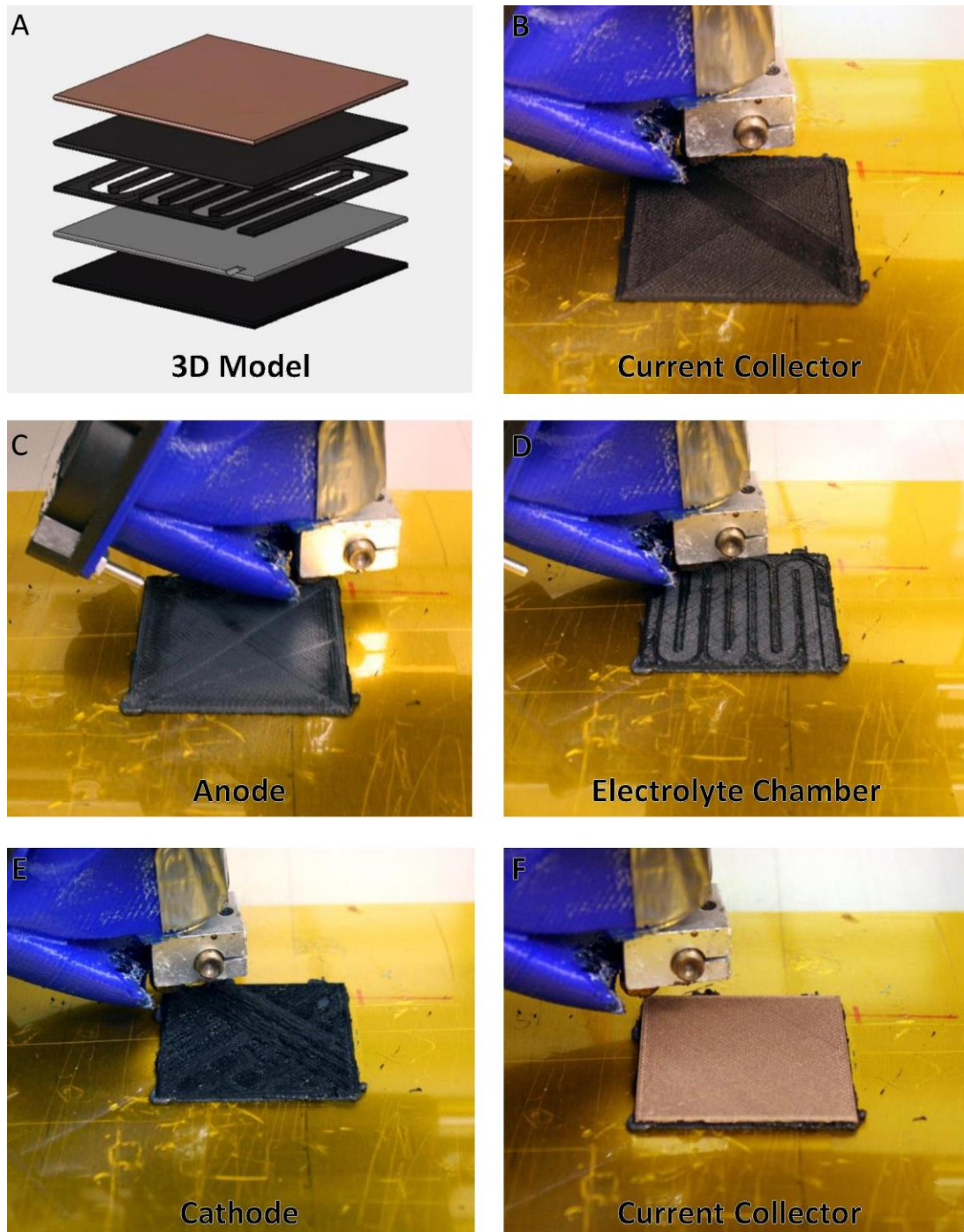


Figure 15. 3D Printing a Single Print Battery. (A) 3D model of the single-print battery. (B) Current collector layer made from Black Magic filament. (C) LTO/graphene/PLA anode layer. (D) The electrolyte layer was printed using pure PLA. (E) LMO/MWNT/PLA cathode layer. (F) Current collector made from Electrifi.

3.5.1 Layer by Layer 3D Printed Lithium Ion Battery Characterization

After printing, the battery was allowed to cool to room temperature and filled with 1M LiClO₄ in 50/50 vol EMC/PC. The battery was allowed to rest for 24 hrs prior to cycling. Following infusion and cycling, the battery was able to power an LED (Figure 16 below). Cycling performance is shown in Figure 11d. The single print battery had a lower capacity (1.16 mAhcm⁻³) than the fully printed and assembled battery (3.91 mAhcm⁻³). The volumetric capacity of the entire single print battery is ~0.1 mAhcm⁻³. This lower capacity relative to the assembled battery may be caused by the inability to completely infuse the anode and cathode with electrolyte.

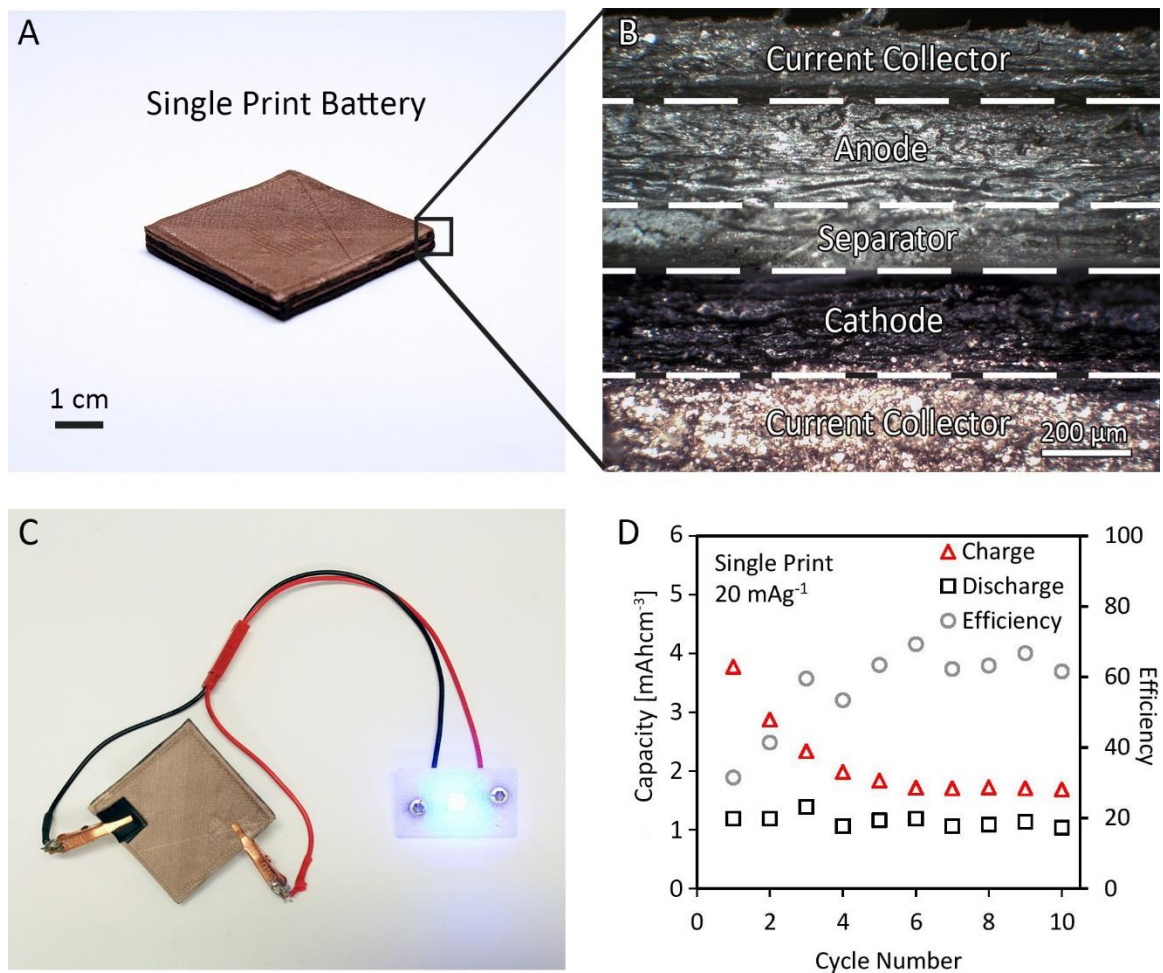


Figure 16. Single Print Battery. (A) A 3D printed battery was printed in a single print by exchanging the filament at predetermined layer heights. The battery was then vacuum filled with electrolyte. (B) Cross sectional 10x microscope image showing the individual layers of the single print battery. (C) Image of 3D printed battery powering an LED. (D) Capacity and coulombic efficiency of the single print battery at a current density of 20 mA g⁻¹ for 10 cycles.

3.6 3D Printed Wearable Lithium Ion Batteries

One of the key benefits of 3D printing is the ability to print arbitrary shapes and sizes. This ability may eventually enable the production of customizable wearable electronics.⁸⁶⁻⁸⁸ To demonstrate this capability, we 3D printed two wearable devices with integrated printed batteries.

3.6.1 3D Printed LED Sunglasses and LED Bangle Bracelet

Figure 6a shows an example of 3D printed LCD sunglasses with 3D printed batteries integrated into the side temples (Figure 17a inset, below). The batteries are connected in series to power an LCD panel that darkens when a voltage is applied by pressing the integrated switch (Figure 17b). The frames and temple arms of the sunglasses were designed as a snap-together case in which the components of the battery and electronics could be inserted. Each component of this battery (anode, cathode and separator) was printed individually and infused with electrolyte prior to assembly into the printed casing. We also demonstrate an LED bangle with an integrated battery in Figure 17 c & d below. For this battery, the anode and cathode were printed as free standing curved electrodes that matched the contour of the bangle (Figure 17c). A Celgard polymer separator (not shown) was used in this device to both improve the performance of the battery as well as demonstrate the ability to integrate 3d printed battery technology with existing materials. After infusion and assembly, the bangle battery could power a green LED for ~60 s. (Figure 17d).

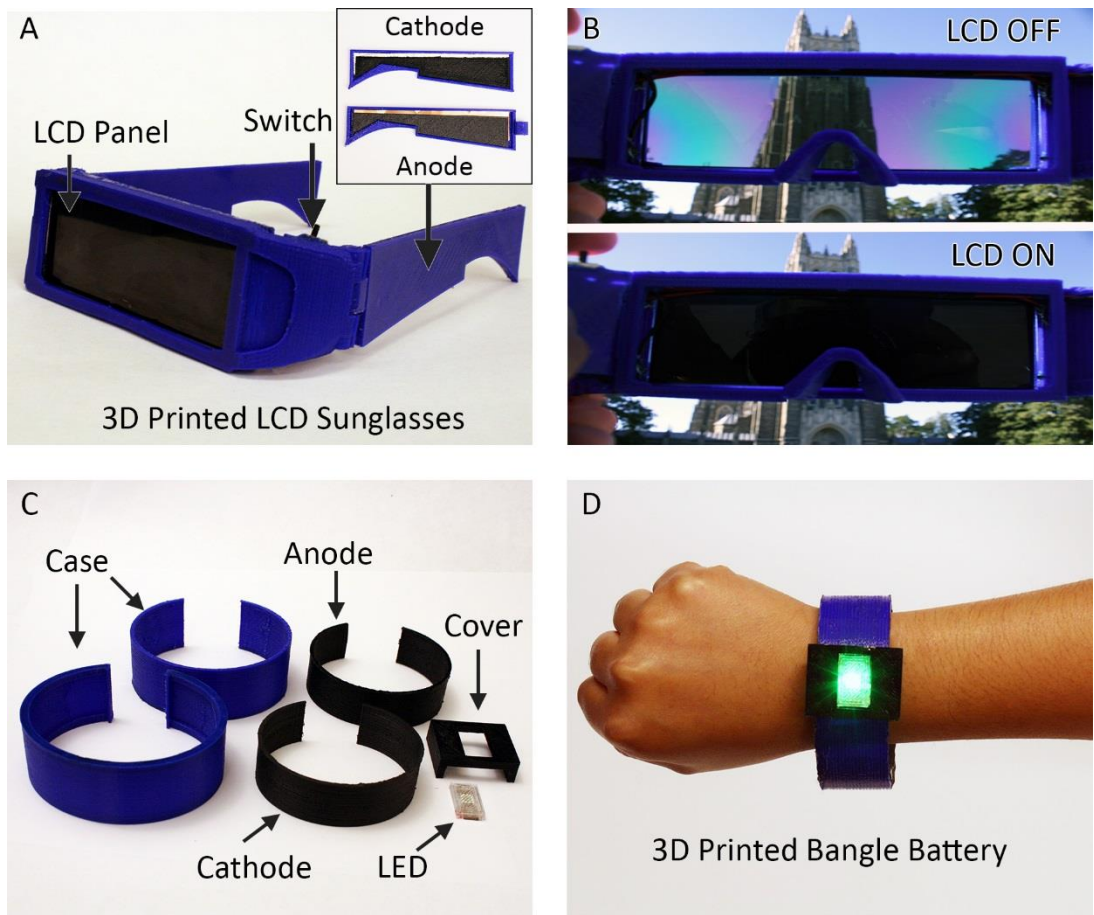


Figure 17. 3D Printed Wearables. (A) 3D printed glasses with an electronic darkening LCD lens and 3D printed batteries integrated into the side temples. (B) Demonstration of the LCD transmitting and blocking an image of the Duke Chapel in the off and on state. (C) Separated view of the internal 3D printed components of a 3D printed bangle battery with an integrated LED. (D) Assembled 3D printed bangle battery powering an LED.

3.7 Summary

The work in this chapter demonstrates that it is possible to 3D print full lithium ion batteries with low-cost fused filament fabrication 3D printers by (1) modifying the most commonly used 3D printing polymer, PLA, to have a similar ionic conductivity to previously reported polymer electrolytes, and (2) creating new polymer composites to enable 3D printing of LIB anodes and cathodes. We found the need to maintain printability limited the amount of conductive filler that could be loaded into the polymer to <30% by volume, and that a maximum battery capacity was achieved at a ratio of 80:20 conductive to active material. This is in contrast to a commercial lithium ion battery, in which the binder is <15% by volume, and the ratio of conductive to active material is ~1:10. Future work may improve upon this initial demonstration by replacing the polymer-based anode and cathode materials with pastes that can accommodate high loadings of active material and be printed in tandem with a polymer separator and case. In addition, the high ionic conductivity of infused PLA suggests the use of this polymer as an electrolyte may be worth additional study. These results should benefit those searching for 3D printable energy storage materials that can be used to create batteries in arbitrary shapes and be integrated with 3D printed electronics.

4. Cu-Ag Core-Shell Nanowire Conductive Filler for Lithium Ion Battery Anodes

In this Chapter, we turn our focus to the electrical conductivity of LIB graphite anodes and examined CuAg NWs with varying aspect ratios as the conductive filler and Super P as the control conductive filler. We also examined the effect of increasing the amount of conductive filler from 1-10% by volume for each sample. It was found that the electronic conductivity and porosity both increased with increasing aspect ratio and volume percent. These increases led to an increase in the gravimetric capacity of the anode. Each sample was cycled at 0.5, 1.0, 4.0 and 10.0 C to investigate the effect on rate performance and anode stability was also examined. It was also found that conventional graphite anodes have performance gains at higher C Rates for all nanowire aspect ratios. One of the key benefits to using CuAg NWs is that they can be processed using aqueous solvents and anodes can be processed with no modification to a traditional anode fabrication process.^{63, 89}

4.1 Fabrication of Nanowire Conductive Filler Anode

Electrodes were fabricated using a conventional slurry doctor blade method for coating copper foil current collectors with our composite anodes.^{90 91-92} The anode slurries were comprised of 325 mesh graphite as the active material, carboxy methyl cellulose (CMC) as the polymer binder and either CuAg NWs or Super P carbon black as the conductive filler. CMC was used in place of conventional polyvinylidene difluoride (PVDF) because of its solubility in water.^{63, 89, 93} Aqueous processability is crucial to our

electrode fabrication as the nanowires are synthesized and stored in an aqueous solution where they remain highly dispersed. Additionally, using an aqueous based slurry reduces the environmental impact caused by the volatile solvents needed to dissolve PVDF. For each anode sample, the volume % of conductive filler tested was 1, 2.5, 5.0 and 10.0 %.

4.1.1 Cu Nanowire Synthesis

We synthesized 2 L batches of Cu nanowires with each reaction formulated to grow nanowires with different lengths and diameters. The synthesis is similar to one developed by Cruz *et al* 2018 (Figure 18 Below) to synthesize gram scale batches of varying aspect ratio nanowires for highly conductive, 3D printable filaments.⁹⁴ After the synthesis, each batch was purified and characterized using dark field microscopy for initial length determination followed by atomic absorption spectroscopy (AAS) to determine nanowire concentration and percent yield. Scanning electron microscopy was then used to precisely determine nanowire diameters and lengths.

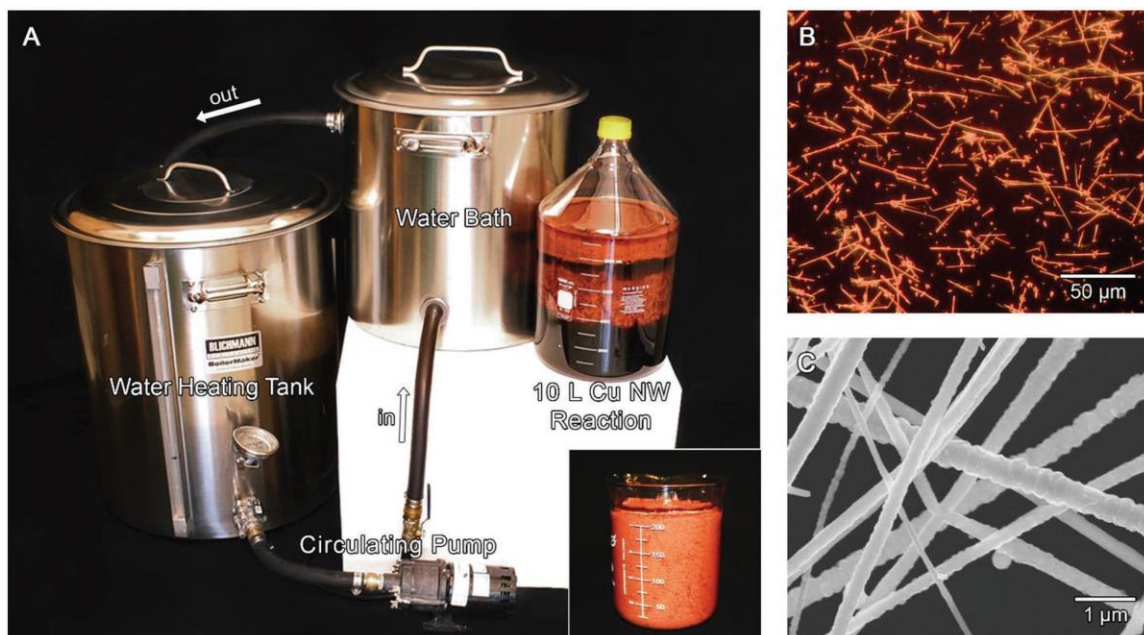


Figure 18. Cu NW Synthesis. A) Circulating water bath setup for the 10 L synthesis of Cu NWs. Inset shows ≈ 22 g of Cu NWs purified from the reaction. B) Dark-field optical microscopy (DFOM) image shows the Cu NWs have an average length of $45 \pm 15 \mu\text{m}$. C) An SEM image shows the Cu NWs have a diameter of $240 \pm 95 \text{ nm}$.⁹⁴

4.1.2 Ag Coating

After characterization, each stock Cu nanowire solution was then diluted or concentrated to 4.4 mg/ml for Ag coating with the final ratio of Cu diameter to Ag thickness calculated to be 85:15. Stewart *et al* 2015 found this ratio was the most resistant to oxidation over time while being subjected to elevated temperature and humidity Figure 19 b and c below.⁹⁵ For each batch of nanowires, the molarity of Ag in the coating solution was modified so that each has a core diameter to shell thickness ratio of 85:15.

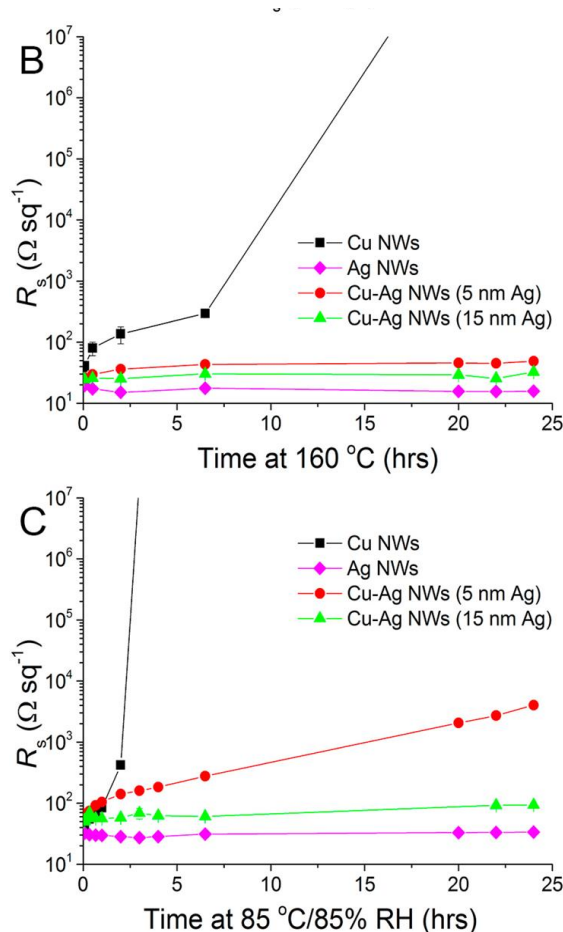


Figure 19. Oxidation Resistance of Cu-Ag Core-Shell. Plots sheet resistance for Cu NWs, Ag NWs, and Cu-Ag NWs with different aspect ratios (L/D) taken from Stewart *et al* 2016. Plots of sheet resistance versus time for Cu NWs, Ag NWs, and Cu-Ag NWs in (B) a dry oven at 160 °C and (C) at 85 °C/85% RH. ⁹⁵

To test the benefits of an oxidation resistant Ag shell on the nanowire, two anode samples were prepared with 5% volume nanowires, one sample with bare Cu NWs and one sample with Ag coated Cu NWs. These samples were cycled a rate of 0.5 C for 50 cycles, Figure 20 below. The bare Cu NWs saw a 74.3% decrease in performance after the 12th cycle and near complete failure by the 43rd cycle. At this point in cycling, the

galvanostat went into over potential protection mode and stopped cycling. The cause of this performance degradation is likely due to oxidation of the bare CuNWs leading to a decrease in conductivity leading to an increase in the potential needed to cycle the anode at a constant current. The Ag coated CuNWs, however, successfully completed 50 cycles with no signs of failure.

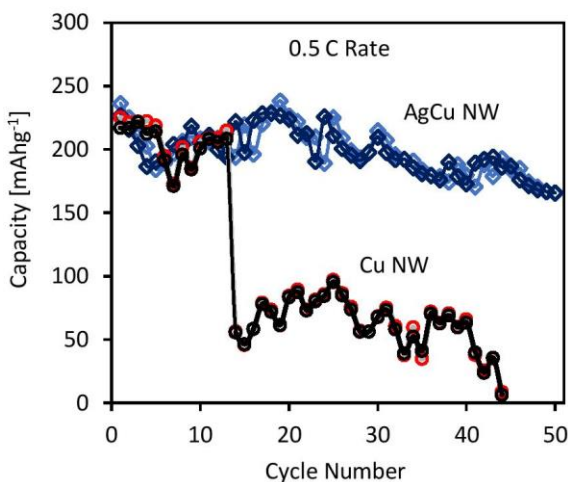


Figure 20. CuAg NW vs Cu NW Anode Stability Comparison. Graphite anodes with 5% Vol Cu NW vs 5% Vol CuAg NW cycled at 0.5 C.

4.1.3 Cu-Ag Core-Shell Nanowire Characterization

After Ag coating, the CuAg nanowires purified once again and examined under SEM to determine length in microns and diameter in nanometers to calculate the aspect ratios of each batch. Table 1 below has the dimensions and labeling system that is used for the remainder of the manuscript.

Table 1 – Nanowire Labels and Dimensions

Sample	L/D	Length	Diameter
11-3	11	$3.1 \pm 0.6 \mu\text{m}$	$298 \pm 30 \text{ nm}$
99-10	99	$10.4 \pm 2.1 \mu\text{m}$	$106 \pm 14 \text{ nm}$
99-34	99	$34.3 \pm 5.7 \mu\text{m}$	$347 \pm 21 \text{ nm}$

Table 1 – Sample labeling scheme with aspect ratios, lengths and diameters of AgCu NWs used as conductive filler in each graphite anode.

4.2 Results for Anode Characterization

In this section we will discuss characterization results from graphite anodes fabricated with CuAg NWs of varying aspect ratio and compare these results to graphite anodes utilizing conductive carbon. We begin with resistivity comparisons for all samples with increasing amounts of conductive filler and then move on to rate performance, cycling stability. Then, we compare gravimetric and volumetric capacity and energy density and finally examine the porosity of a subset of samples.

4.2.1 Anode Fabrication and Resistivity

The target thickness for all anode samples was $100 \mu\text{m}$ as to maximize energy density.^{5-6, 89, 96-98} Figure 21 below shows a topside view of anodes with 1.0, 2.5, 5.0 and 10.0% volume 99-34 nanowires.

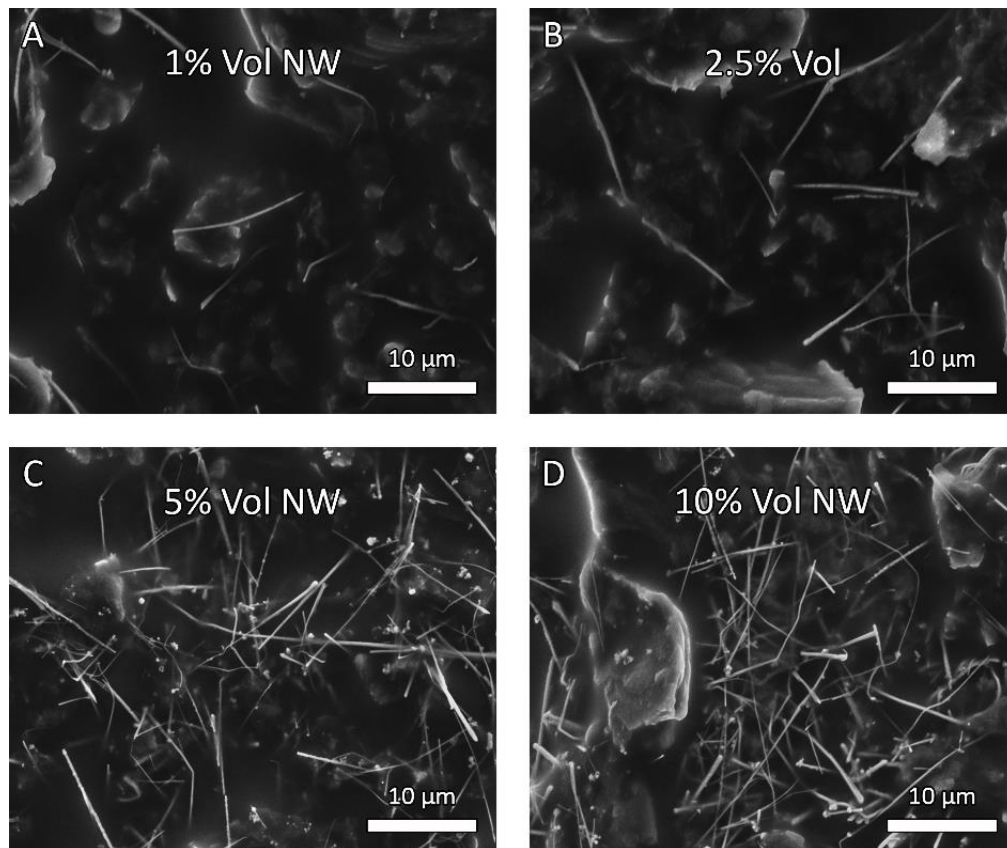


Figure 21. Anode Aerial SEM Images. Graphite anodes with increasing volume percent of sample 99-34 CuAg nanowires from 1-10%, A-D. Nanowires shown in are from sample 99-34.

Figure 22 below shows a cross section SEM image of a 5 % vol nanowire sample 11-3 (Fig 22A) and a 5% vol nanowire sample 99-34 (Fig 22B). It can be seen in Figure 22A and B that the nanowires are well distributed throughout the anodes. The smallest aspect ratio nanowires (11-3) are distributed between and around graphite particles similarly to the distribution of conventional carbon black. The largest aspect ratio nanowires (99-34) can be seen spanning several graphite particles as well as bridging long gaps. Figure 22 C plots of the length and diameters are shown with the nanowire labels. Longer, thinner

nanowires with much higher aspect ratios can be synthesized but cannot be Ag coated due to formulation of the reaction solution and the capping agent preventing Ag deposition. It is also assumed that higher aspect ratio nanowires would suffer from aggregation and breakage during the slurry fabrication process. The resistivity of each anode sample was tested using a 4-point probe method (Fig 22D). With each sample, the resistivity of the anode decreased with increasing volume % of conductive filler. All nanowire samples had resistivities lower than the Super p samples at any volume percent. The resistivity of anodes with nanowires decreased with increasing length. For all samples, there was a significant decrease in resistivity when increasing the volume % of conductive filler from 1- 5%. There was less of a decrease in resistivity when increasing the volume % of conductive filler from 5-10%. At 5% volume percent, anode samples with 99-34 nanowires had a resistivity over 500x lower than the anode samples with Super P. The decrease in resistivity can be attributed to the increased conductivity of the CuAg NW compared to carbon black and the distribution of nanowires in the anodes.

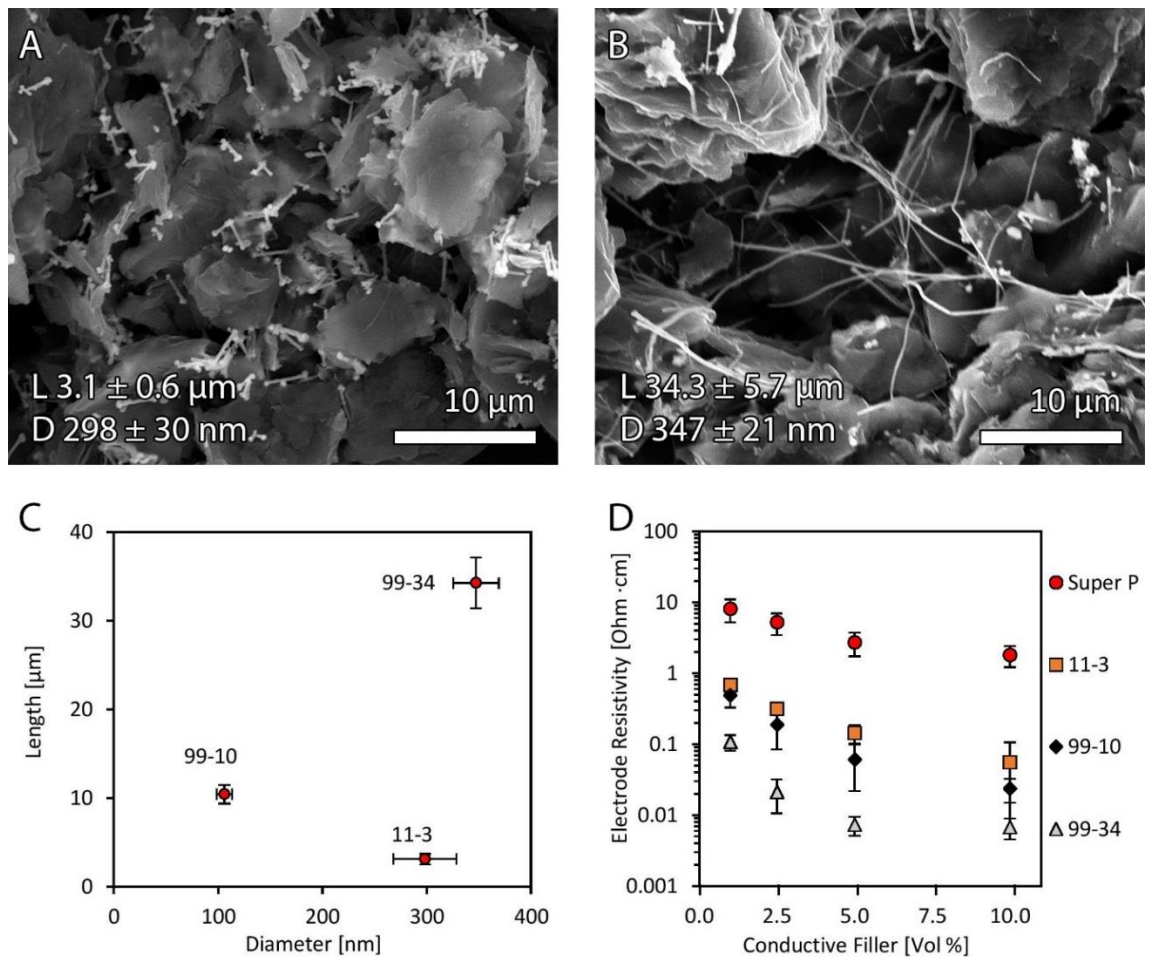


Figure 22. Anode Cross Sections, Aspect Ratios and Resistivities. A) Cross section of anode with 5% Vol CuAg NW sample 11-3. B) Cross section of anode with 5% Vol CuAg NW sample 99-34. C) Length in μm versus diameter in nm for nanowires used each sample of electrodes with sample labels. D) Electrode resistivity versus volume % of conductive filler for each aspect ratio.

4.2.2 Anode Rate Performance

After examining resistivity, each anode sample was galvanostatically tested to investigate capacity and rate performance. Each half cell consisted of the graphite-based anode, Celgard 25 μm polypropylene (PP) separator, 1M lithium hexafluorophosphate

(LiPF₆) in 50/50 vol Diethyl Carbonate (DEC) and Ethylene Carbonate (EC) and lithium metal as the counter electrode. Each sample was cycled at increasing C Rates (0.5, 1.0, 4.0, 10.0 C) to investigate the effect of aspect ratio and volume percent on rate performance (Figure 23 below). For each sample, there was increase in capacity with an increase in conductive filler for all C Rates due the increase in electron transport.^{45, 99-100} Higher aspect ratio samples, 99-10 and 99-34, outperformed Super P and 11-3 samples at all volume % and C Rates. This is an effect of higher aspect ratio nanowires allowing for lower resistivities, leading to more efficient electron transport. At the same aspect ratio, 99, the samples with the shorter lengths, 10 μm vs 34 μm , performed better at all C Rates and all volume percent. One possible reasoning for the increase in performance with decreasing length, but same aspect ratio, is the distribution of nanowires throughout the electrode. The 99-34 nanowires are ~3 times larger in diameter (377 vs 106 nm) and ~3 times longer (34.3 vs 10.4 μm). This equates to samples 99-10 having ~40 times more nanowires per volume compared to samples 99-34 at equivalent volume percent.

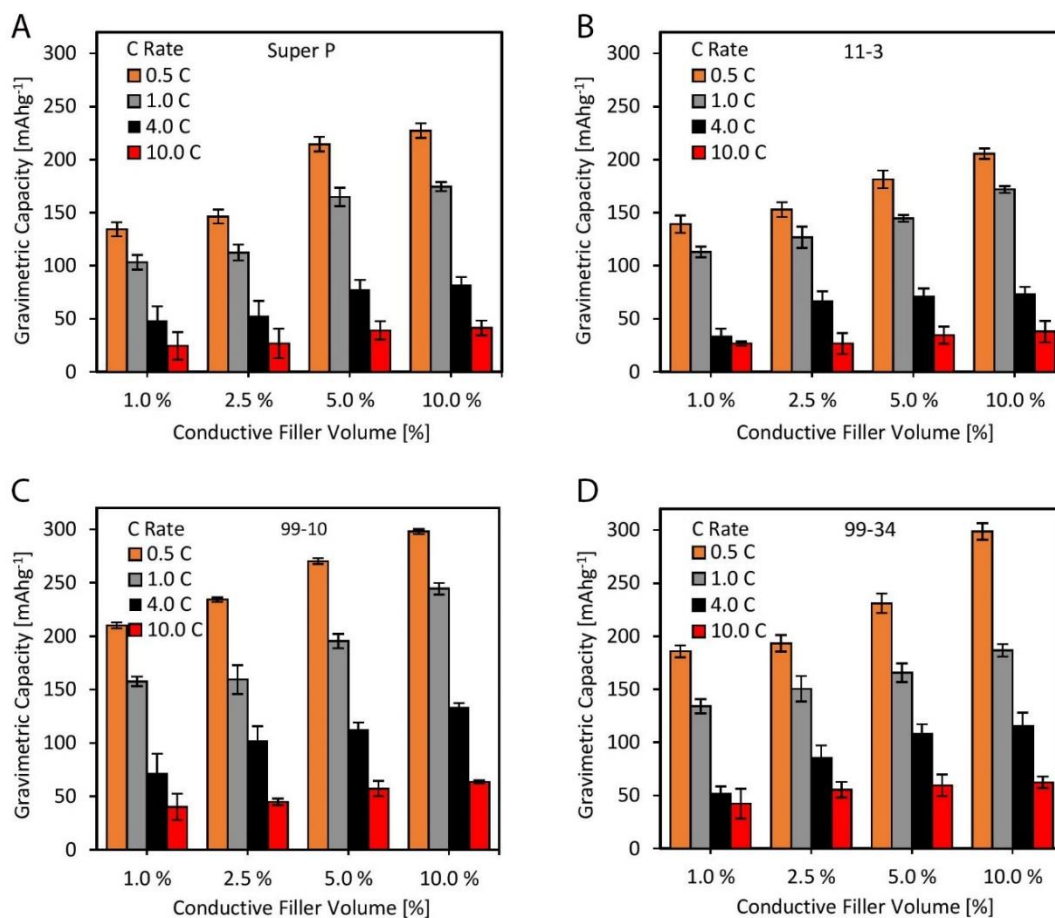


Figure 23. Gravimetric Capacities. A-D) Gravimetric capacity, active mass normalized, versus volume percent of conductive filler (1-10%) with increasing C Rate (0.5, 1.0, 4.0, 10.0C) for anodes samples A) Super P, B) 11-3, C) 99-10, D) 99-34.

4.2.3 Performance Increase and Cycling Stability

To elucidate the actual increase in performance, we plotted the capacity performance gain of each nanowire sample with respect to the Super P sample under exact conditions (Figure 24 below). It was found that sample 99-34 had the biggest increases in capacity performance at any C-Rate and volume percent. The biggest gains, 90-95%, were achieved at 2.5 Vol% 99-34 at 4C and 10C respectively. This is due to the increased

conductivity allowing for efficient electron transport and the increased porosity allowing for enhanced ion transport. Sample 11-3 had the worst performance increases followed by 99-10 having the second-best increases.

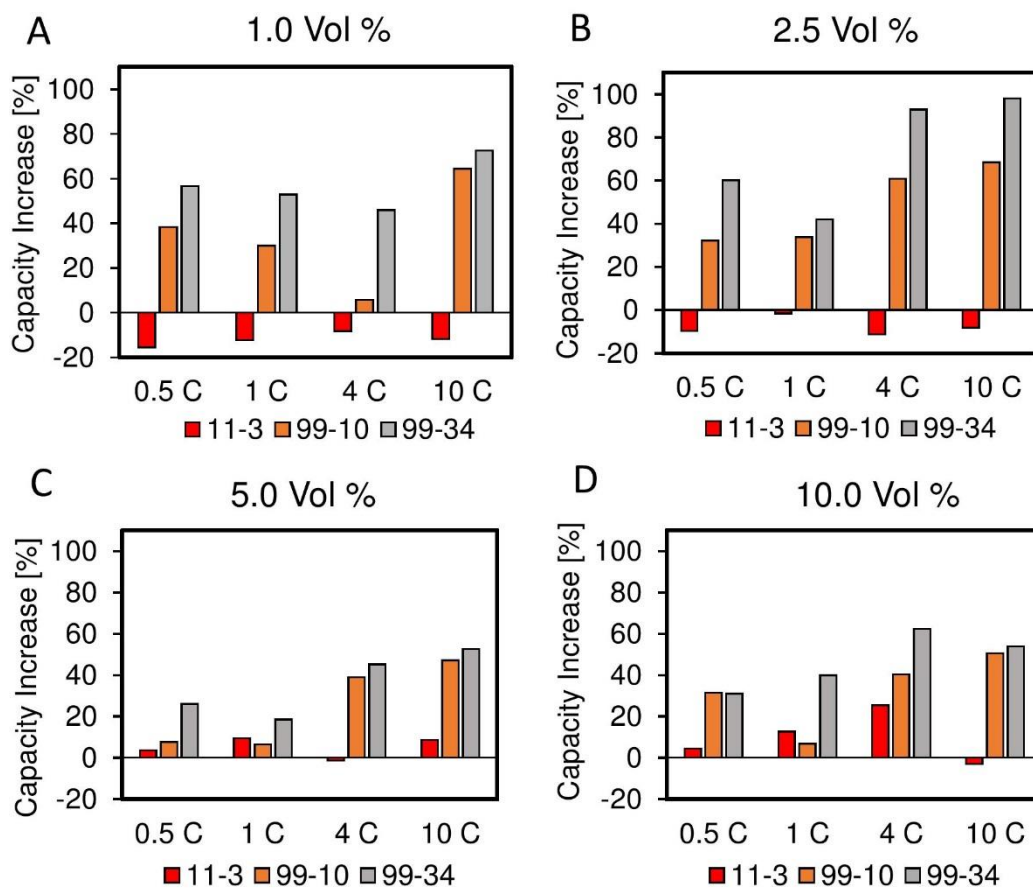


Figure 24. Capacity Increases. A) and B) Charge and discharge voltage curves for anodes with 5% volume Super P, 99-34 NWs and 11-3 NWs at a rate of 1.0C. C) Gravimetric capacity, active material normalized, versus cycle number for anodes with 5% volume Super P, 99-34 NWs and 11-3 NWs at a rate of 1.0C. D) Volumetric energy density, full cell, versus cycle number for anodes with 5% volume Super P, 99-34 NWs and 11-3 NWs at a rate of 1.0C.

Following rate testing, the samples were cycled 50 times at 1.0 C to examine the stability of CuAg NWs as a conductive filler (Figure 25 below). There is a significant increase in the voltage vs capacity for 11-3 and a slight increase for Super P. The capacity of samples 99-34, Super P, and 11-3 were stable over 50, 1.0 C cycles and maintained columbic efficiencies above 95% (not shown) with no signs of degradation. Samples 99-34, Super P, and 11-3 had capacities of 195.4, 155.5 and 143.9 mahg⁻¹ respectively, averaged over 50 cycles. The capacity of sample 99-10 decreased 45.8% from 275.8 mahg⁻¹ at cycle 1 to 149.3 mahg⁻¹ at cycle 50 Figure 19 below. This degradation in performance is attributed to the small diameter of the nanowires in sample 99-10 (106 nm) as samples 99-34 and 11-3 were stable and had diameters of 377 nm and 298 nm respectively. To confirm this hypothesis, CuAg NWs were synthesized with a length of 3.6 μm and a diameter of 70.3 nm (sample 50-3) then tested in a graphite anode at 5% vol at 0.5 C for 50 cycles. The capacity of sample 50-3 degraded after 7 cycles and did not begin to stabilize until the 30th cycle. The capacity then decreased at a similar rate as sample 99-10 for the last 20 cycles. Rate performance test were performed on separate 50-3 samples and all displayed capacity degradation at all C Rates (0.5, 1.0, 4.0, 10.0C). The mechanism for this failure is not yet clear as sample 50-3 also had a Cu to Ag ratio of 85:15 but may be a function of shell thickness as the thinner diameter wires have a smaller shell.

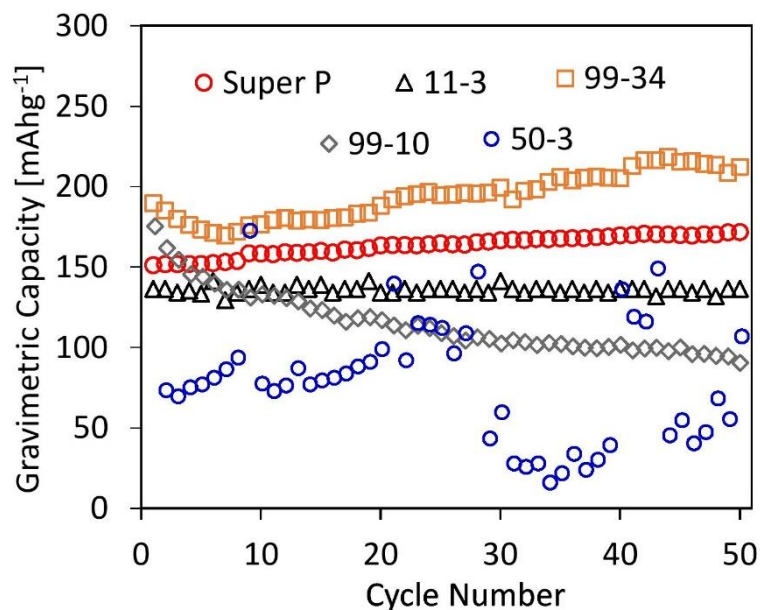


Figure 25. Anode Cycling Stability. A) Gravimetric capacity, active material normalized, versus cycle number for anodes with 5% volume Super P, 11-3, 50-3, 99-10, 99-34.

4.2.4 Anode Porosity and Composition

In this section, we examine the effect of aspect ratio on the porosity and composition of the anode. Work by Catenacci *et al* 2018, have demonstrated that aerogels made from Cu nanowires show decreasing density with increasing aspect ratio. Figure 26 below show Cu nanowires of increasing aspect ratio settled in solution next to aerogels made from these solutions, all with the same mass of Cu nanowires. The change in density or increase in porosity can be seen as the thickness of each aerogel increases as the aspect ratio increases, at the same mass of nanowires.

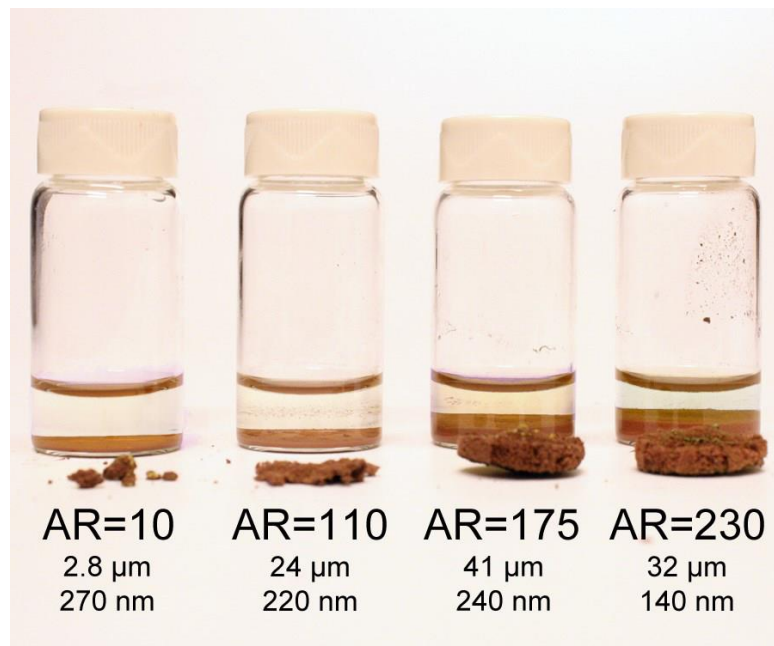


Figure 26. CuAg NW Aerogels. Photograph of settled Cu-Ag NWs in solution and subsequent aerogels formed after freeze-drying. Image - M. Catenacci 2018

To that effect, we measured the porosity of anodes with 5% volume conductive fillers - Super P, 11-3, 99-10, 99-34. The porosity was determined by comparing the measured volume of the electrodes with the expected volume as calculated using the mass of the electrode and the calculated volume of solids based on the weight percent of solids. Figure 27 A below, show the average porosities of anode samples Super P, 11-3, 99-10 and 99-34. There is an increase in porosity with increasing aspect ratio, supporting our hypothesis that the density of our high aspect ratio samples is lower, leading to lower energy densities.

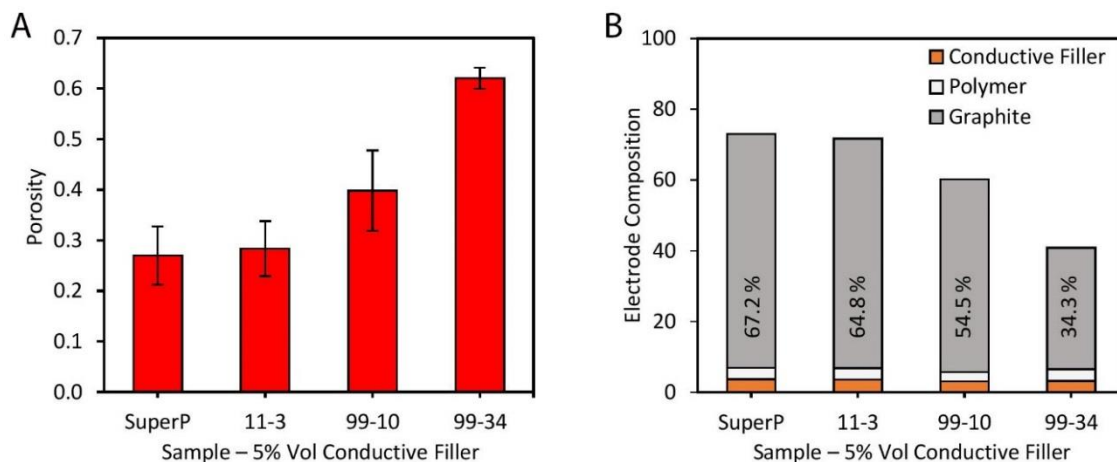


Figure 27. Porosity and Electrode Composition. A) Porosity comparison of samples containing 5% Vol conductive filler. B) Electrode composition comparison of samples containing 5% Vol conductive filler.

As the porosity of the anode increases, the volume of solids – active material, conductive filler and polymer binder, decrease. Figure 27 B above, shows the anode composition in volume percent. There is a significant decrease in the volume percent of the active material, graphite, as the aspect ratio increases. The volume percent of graphite decreases slightly from Super P (67.2%) to 11-3 (64.8%). For samples 99-10 and 99-34, the volume percent decrease of graphite is more significant, 54.5% and 34.3% respectively. The decrease in the volume percent of solids explains the decrease in energy density for the larger aspect ratio as their electrode densities are lower than Super P and 11-3 anode samples.

4.2.5 Effect of Aspect Ratio and Porosity on Internal Resistance

To understand the effects of aspect ratio and porosity, we examined each 5% Vol nanowire samples using EIS to measure the SEI and charge transfer resistance. We tested samples 99-34, 99-10, 11-3 and Super P using a two electrode EIS set up with lithium as the counter electrode and 1M LiPF₆ in EC/PC as the electrolyte with a 25 μm polypropylene separator. The EIS experiments were performed from 100 kHz to 0.1 Hz at 10 mVpp. Each sample was subjected to an SEI formation cycle prior to measurement. Figure 23 below has a Nyquist example of sample 99-34 and Super P (Figure 28 below). It can be seen that the 99-34 nanowires have a significant improvement over the Super P sample in the charge transfer resistance, 24.14 Ω and 163.3 Ω respectively.

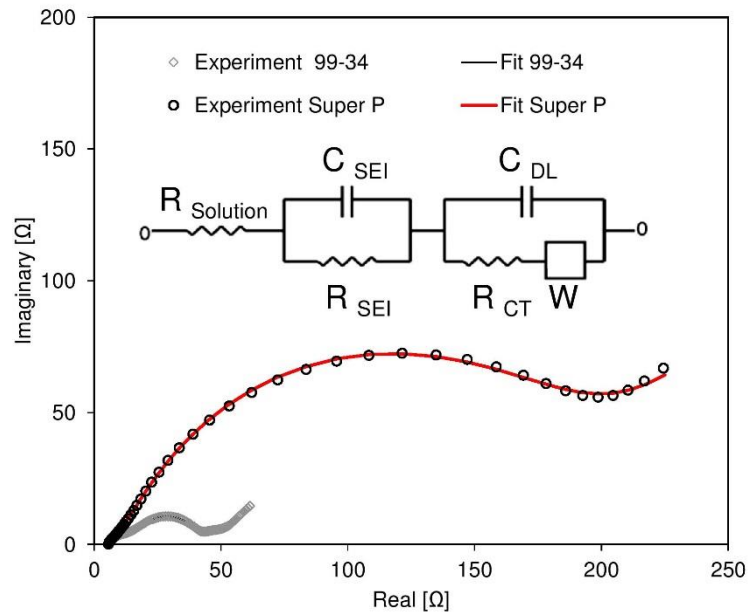


Figure 28. Nyquist plot of Anodes. EIS scan and fit for 5 vol % Super P and 99-34. Inset is the equivalent circuit used to model the fit.

We compared the charge transfer resistances (Figure 29A) of each sample and found that there is a decrease in charge transfer resistance with increasing aspect ratio and length. This is similar in trend to the resistivity decrease results of each sample at 5% vol. The decrease in charge transfer resistance of the nanowire samples compared to Super P is the increased electron transfer efficiency caused by the increased conductivity of the nanowires and the length. We also extracted the SEI resistances for each sampled and plotted them against the porosity of each sample (Figure 29B).

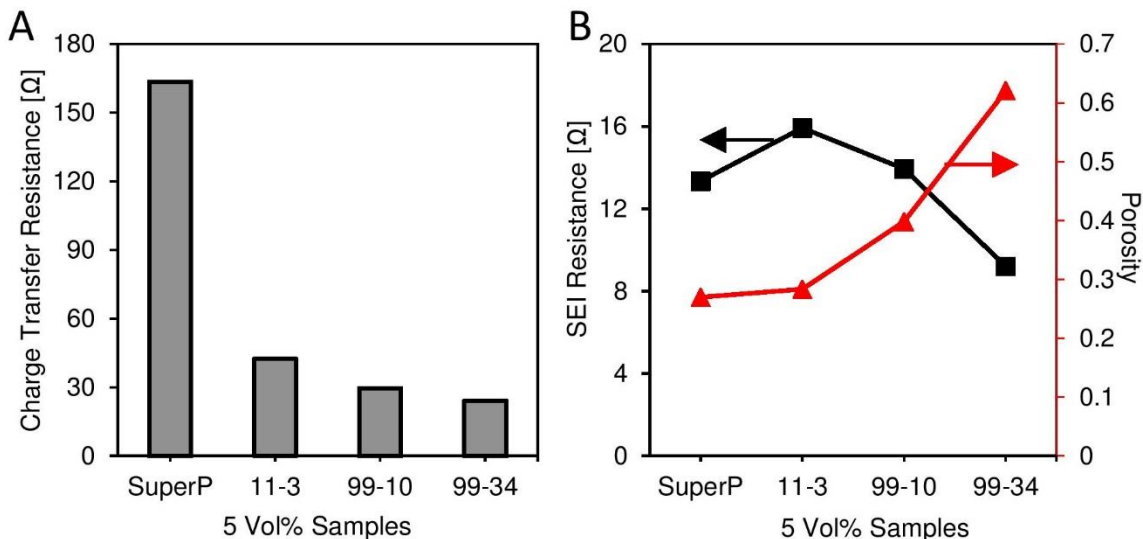


Figure 29. Charge Transfer and SEI Resistance. A) Comparison of the charge transfer resistance and conductive filler sample. B) Comparison of SEI Resistance and porosity of each samples.

There appears to be a decrease in SEI resistance with increasing porosity of each electrode. We hypothesis that the decrease of SEI resistance is due to a decrease in SEI thickness. Increased porosity equates to an increased surface area within the electrode. The SEI is formed in each sample at the same formation conditions, 24 aging followed by 12 hr

formation charge and a subsequent 12 hr discharge. Assuming that the same amount of lithium is consumed during the formation process, electrodes with a smaller porosity and thus smaller surface area will have a thicker SEI layer than that of a high porosity, high surface area with the same amount of SEI deposition. Further analysis of the SEI layer and resistivity is needed to fully confirm this hypothesis.

4.3 Summary

In conclusion, the research in this chapter demonstrated the ability to use Cu-Ag core-shell nanowires as a high-performance substitute for conventional carbon black in graphite-based lithium ion batteries. Furthermore, we show that the aspect ratio of the CuAg NWs effects the performance as increasing the aspect ratio increases both electrical conductivity and porosity. We found that increasing the amount of conductive filler from 1-10% volume increases the electrical conductivity and capacity of the anode. Both aspect ratio and volume percent of nanowires both enhance the rate performance of the anode, but at the cost of energy density. Future work in nanowires as conductive fillers could explore a wider range of aspect ratios and test the effects of different Ag shell thicknesses.

5. Conclusion

In conclusion, the field of lithium ion batteries will continue to transform as industries such as electric vehicles, renewable energy storage and portable electronics continuously demand higher capacities and energy densities. We discussed advanced fabrication techniques and previous works whose goal were to increase the energy density

of lithium ion batteries for various applications. In Chapter 2, I demonstrated a complete LIB fabricated using Fused Filament Fabrication (FFF), or more commonly known as 3D printing. In the development of 3D printable LIBs, we discovered key metrics that enable this technology, mainly electrical conductivity and printability. I also demonstrated the ability to print a complete LIB in one print as well as the ability to 3D print wearable devices with integrated 3D printed LIBs. The capacity of the 3D printed LIBs was 1-2% of a conventional LIB, due to the low active filler content. Although the ionic and electrical conductivity of my 3D printed LIBs was comparable to conventional LIBs, the amount of polymer binder prohibited the active material to contact both the conductive filler and the electrolyte infused polymer simultaneously. I believe this issue can be resolved by using an active material that is higher in electrical conductivity and has a morphology that allows for better electrical contact with the conductive filler, such as a nanowire or nanotube. If this can be achieved, we should be able to completely 3D print LIBs that can perform as well as conventionally manufactures ones. After understanding the importance of efficient electron transport, I turned my focus In Chapter 3 to improving the electronic conductivity of a conventional anode. Here, I showed Cu-Ag core-shell nanowires can be used as a replacement for carbon as the conductive additive in a conventional graphite LIB anode. In particular, I investigated the effect of aspect ratio on several performance metrics including rate performance as well as gravimetric and volumetric capacity and energy density. It was discovered that increasing the aspect ratio

enhances rate performance as electrical conductivity is increased. Future work in Cu-Ag NW conductive fillers should examine the cathodic stability for use in conventional LIB cathodes, further enhancing the performance of an LIB and possibly lead to commercialization of this technology. Overall, this thesis has shown the ability to 3D print a lithium ion battery and has reinforced the importance of electronic conductivity to the performance of any LIB, regardless of manufacturing method.

References

1. Blomgren, G. E., The development and future of lithium ion batteries. . *Journal of The Electrochemical Society* **2017**, 164 (1), A5019-A5025.
2. Yazami, R. a. T., P. , A reversible graphite-lithium negative electrode for electrochemical generators. *Journal of Power Sources* **1983**, 9 (3), 365-371.
3. Fleming, B., An Overview of Advances in Automotive Electronics. *IEEE Vehicular Technology Magazine* **2014**, 9 (1), 4-9.
4. Asp, L. E.; Greenhalgh, E. S., Structural power composites. *Composites Science and Technology* **2014**, 101, 41-61.
5. Singh, M., Kaiser, J., & Hahn, H., Thick Electrodes for High Energy Lithium Ion Batteries. *Journal of The Electrochemical Society* **2015**, 162 (7), A1196-A1201.
6. Danner, T.; Singh, M.; Hein, S.; Kaiser, J.; Hahn, H.; Latz, A., Thick electrodes for Li-ion batteries: A model based analysis. *Journal of Power Sources* **2016**, 334, 191-201.
7. Shirshova, N.; Qian, H.; Shaffer, M. S. P.; Steinke, J. H. G.; Greenhalgh, E. S.; Curtis, P. T.; Kucernak, A.; Bismarck, A., Structural composite supercapacitors. *Composites Part A: Applied Science and Manufacturing* **2013**, 46, 96-107.
8. Fu, K.; Wang, Y.; Yan, C.; Yao, Y.; Chen, Y.; Dai, J.; Lacey, S.; Wang, Y.; Wan, J.; Li, T.; Wang, Z.; Xu, Y.; Hu, L., Graphene Oxide-Based Electrode Inks for 3D-Printed Lithium-Ion Batteries. *Adv Mater* **2016**, 28 (13), 2587-94.
9. Singh, M.; Kaiser, J.; Hahn, H., Thick Electrodes for High Energy Lithium Ion Batteries. *Journal of the Electrochemical Society* **2015**, 162 (7), A1196-A1201.
10. Ho, C. C.; Murata, K.; Steingart, D. A.; Evans, J. W.; Wright, P. K., A super ink jet printed zinc-silver 3D microbattery. *Journal of Micromechanics and Microengineering* **2009**, 19 (9), 094013.
11. Hu, J.; Jiang, Y.; Cui, S.; Duan, Y.; Liu, T.; Guo, H.; Lin, L.; Lin, Y.; Zheng, J.; Amine, K.; Pan, F., 3D-Printed Cathodes of LiMn_{1-x}Fe_xPO₄Nanocrystals Achieve Both Ultrahigh Rate and High Capacity for Advanced Lithium-Ion Battery. *Advanced Energy Materials* **2016**, 6 (18), 1600856.

12. Li, Q.; Zhu, S.; Lu, Y., 3D Porous Cu Current Collector/Li-Metal Composite Anode for Stable Lithium-Metal Batteries. *Advanced Functional Materials* **2017**, *27* (18), 1606422.
13. Roberts, M.; Johns, P.; Owen, J.; Brandell, D.; Edstrom, K.; El Enany, G.; Guery, C.; Golodnitsky, D.; Lacey, M.; Lecoeur, C.; Mazor, H.; Peled, E.; Perre, E.; Shaijumon, M. M.; Simon, P.; Taberna, P.-L., 3D lithium ion batteries— from fundamentals to fabrication. *Journal of Materials Chemistry* **2011**, *21* (27), 9876.
14. Sun, K.; Wei, T. S.; Ahn, B. Y.; Seo, J. Y.; Dillon, S. J.; Lewis, J. A., 3D printing of interdigitated Li-ion microbattery architectures. *Adv Mater* **2013**, *25* (33), 4539-43.
15. Foster, C. W.; Down, M. P.; Zhang, Y.; Ji, X.; Rowley-Neale, S. J.; Smith, G. C.; Kelly, P. J.; Banks, C. E., 3D Printed Graphene Based Energy Storage Devices. *Sci Rep* **2017**, *7*, 42233.
16. Wei, M.; Zhang, F.; Wang, W.; Alexandridis, P.; Zhou, C.; Wu, G., 3D direct writing fabrication of electrodes for electrochemical storage devices. *Journal of Power Sources* **2017**, *354*, 134-147.
17. Kohlmeyer, R. R.; Blake, A. J.; Hardin, J. O.; Carmona, E. A.; Carpena-Núñez, J.; Maruyama, B.; Daniel Berrigan, J.; Huang, H.; Durstock, M. F., Composite batteries: a simple yet universal approach to 3D printable lithium-ion battery electrodes. *J. Mater. Chem. A* **2016**, *4* (43), 16856-16864.
18. Blake, A. J.; Kohlmeyer, R. R.; Hardin, J. O.; Carmona, E. A.; Maruyama, B.; Berrigan, J. D.; Huang, H.; Durstock, M. F., 3D Printable Ceramic-Polymer Electrolytes for Flexible High-Performance Li-Ion Batteries with Enhanced Thermal Stability. *Advanced Energy Materials* **2017**, *7* (14), 1602920.
19. Kil, E. H.; Choi, K. H.; Ha, H. J.; Xu, S.; Rogers, J. A.; Kim, M. R.; Lee, Y. G.; Kim, K. M.; Cho, K. Y.; Lee, S. Y., Imprintable, bendable, and shape-conformable polymer electrolytes for versatile-shaped lithium-ion batteries. *Adv Mater* **2013**, *25* (10), 1395-400.
20. Kim, S. H.; Choi, K. H.; Cho, S. J.; Choi, S.; Park, S.; Lee, S. Y., Printable Solid-State Lithium-Ion Batteries: A New Route toward Shape-Conformable Power Sources with Aesthetic Versatility for Flexible Electronics. *Nano Lett* **2015**, *15* (8), 5168-77.

21. Snyder, J. F., Carter, R. H., Xu, K., Wong, E. I., Nguyen, P. A., Hgo, E. H., & Wetzal, E. D., Multifunctional Structural Composite Batteries for U.S. Army Applications. *Army research lab aberdeen proving ground MD* **2007**, (No. ARL-RP-193).
22. Kjell, M. H., Jacques, E., Zenkert, D., Behm, M., & Lindbergh, G., PAN-Based Carbon Fiber Negative Electrodes for Structural lithium-ion batteries. *Journal of the Electrochemical Society* **2011**, *158* (12), A1455-A1560.
23. Deka, B. K.; Hazarika, A.; Kim, J.; Park, Y.-B.; Park, H. W., Recent development and challenges of multifunctional structural supercapacitors for automotive industries. *International Journal of Energy Research* **2017**, *41* (10), 1397-1411.
24. Mullenax, J., Browning, P., Huebsch, W., Gautam, M., & Sabolsky, E. M. , Composite Multifunctional Lithium Ion Batteries. *ECS Transactions* **2012**, *41* (41), 175-185.
25. Al-Salman, R.; Sommer, H.; Brezesinski, T.; Janek, J., Template-Free Electrochemical Synthesis of High Aspect Ratio Sn Nanowires in Ionic Liquids: A General Route to Large-Area Metal and Semimetal Nanowire Arrays? *Chemistry of Materials* **2015**, *27* (11), 3830-3837.
26. Schwingshackl, C. W.; Aglietti, G. S.; Cunningham, P. R., Experimental Determination of the Dynamic Behavior of a Multifunctional Power Structure. *AIAA Journal* **2007**, *45* (2), 491-496.
27. Ferreira, A. D. B. L.; Nóvoa, P. R. O.; Marques, A. T., Multifunctional Material Systems: A state-of-the-art review. *Composite Structures* **2016**, *151*, 3-35.
28. Sairajan, K. K.; Aglietti, G. S.; Mani, K. M., A review of multifunctional structure technology for aerospace applications. *Acta Astronautica* **2016**, *120*, 30-42.
29. Wang, X.; Jiang, M.; Zhou, Z.; Gou, J.; Hui, D., 3D printing of polymer matrix composites: A review and prospective. *Composites Part B: Engineering* **2017**, *110*, 442-458.
30. Espalin, D.; Muse, D. W.; MacDonald, E.; Wicker, R. B., 3D Printing multifunctionality: structures with electronics. *The International Journal of Advanced Manufacturing Technology* **2014**, *72* (5-8), 963-978.

31. Gnanasekaran, K.; Heijmans, T.; van Bennekom, S.; Woldhuis, H.; Wijnia, S.; de With, G.; Friedrich, H., 3D printing of CNT- and graphene-based conductive polymer nanocomposites by fused deposition modeling. *Applied Materials Today* **2017**, *9*, 21-28.
32. Ladd, C.; So, J. H.; Muth, J.; Dickey, M. D., 3D printing of free standing liquid metal microstructures. *Adv Mater* **2013**, *25* (36), 5081-5.
33. Parekh, D. P., Cormier, D. & Dickey, M. D., Multifunctional Printing Incorporating Electronics into 3D Parts Made by Additive Manufacturing. *Additive Manufacturing* **2015**, 215
34. Aravindan, V.; Gnanaraj, J.; Madhavi, S.; Liu, H. K., Lithium-ion conducting electrolyte salts for lithium batteries. *Chemistry* **2011**, *17* (51), 14326-46.
35. Croce, F., Appetecchi, G. B., Persi, L., & Scrosati, B. , Nanocomposite polymer electrolytes for lithium ion batteries. *Nature* **1998**, *394* (6692), 456-458.
36. J.Y. Song, Y. Y. W., C.C. Wan, Review of gel-type polymer electrolytes for lithium-ion batteries. *journal of Power Sources* **1997**, *77*, 173-197.
37. Koksang, R., Olsen, I. I., & Shackle, D., Review of hybrid polymer electrolytes and rechargeable lithium batteries. *Solid State Ionics* **1994**, *69* (3), 320-335.
38. Manuel Stephan, A., Review on gel polymer electrolytes for lithium batteries. *European Polymer Journal* **2006**, *42* (1), 21-42.
39. Manuel Stephan, A.; Nahm, K. S., Review on composite polymer electrolytes for lithium batteries. *Polymer* **2006**, *47* (16), 5952-5964.
40. Meyer, W. H., Polymer Electrolytes for Lithium-Ion Batteries. *Advanced materials* **1998**, *10* (6), 439-448.
41. K.W.Chew*, T. C. N. a. Z. H. H., Conductivity and Microstructure Study of PLA-Based Polymer Electrolyte Salted With Lithium Perchloride, LiClO₄. *Int. J. Electrochem. Sci.* **2013**, *8* 6354 - 6364.
42. Chew, K. W., Development of Novel Bio-Degradable Electrolyte Based on Polylactide (PLA) for Lithium Rechargeable Battery. *Chew, K. W.* **2014**, *Advanced Materials Research* (853), 270-275.

43. Sabzi, M.; Jiang, L.; Liu, F.; Ghasemi, I.; Atai, M., Graphene nanoplatelets as poly(lactic acid) modifier: linear rheological behavior and electrical conductivity. *Journal of Materials Chemistry A* **2013**, *1* (28), 8253.
44. Shen, Y.; Jing, T.; Ren, W.; Zhang, J.; Jiang, Z.-G.; Yu, Z.-Z.; Dasari, A., Chemical and thermal reduction of graphene oxide and its electrically conductive polylactic acid nanocomposites. *Composites Science and Technology* **2012**, *72* (12), 1430-1435.
45. Park, M.; Zhang, X.; Chung, M.; Less, G. B.; Sastry, A. M., A review of conduction phenomena in Li-ion batteries. *Journal of Power Sources* **2010**, *195* (24), 7904-7929.
46. Campion, C. L.; Li, W.; Euler, W. B.; Lucht, B. L.; Ravdel, B.; DiCarlo, J. F.; Gitzendanner, R.; Abraham, K. M., Suppression of Toxic Compounds Produced in the Decomposition of Lithium-Ion Battery Electrolytes. *Electrochemical and Solid-State Letters* **2004**, *7* (7), A194.
47. Thackeray, M. M.; Wolverton, C.; Isaacs, E. D., Electrical energy storage for transportation—approaching the limits of, and going beyond, lithium-ion batteries. *Energy & Environmental Science* **2012**, *5* (7), 7854.
48. Wang, C., Appleby, A.J. and Little, F.E., Charge–discharge stability of graphite anodes for lithium-ion batteries. *Journal of Electroanalytical Chemistry* **2001**, 497 (1-2).
49. Lu, M.; Cheng, H.; Yang, Y., A comparison of solid electrolyte interphase (SEI) on the artificial graphite anode of the aged and cycled commercial lithium ion cells. *Electrochimica Acta* **2008**, *53* (9), 3539-3546.
50. Qi, X. Y.; Yan, D.; Jiang, Z.; Cao, Y. K.; Yu, Z. Z.; Yavari, F.; Koratkar, N., Enhanced electrical conductivity in polystyrene nanocomposites at ultra-low graphene content. *ACS Appl Mater Interfaces* **2011**, *3* (8), 3130-3133.
51. Julien, C. M., Mauger, A., Zaghib, K., & Groult, H., Comparative Issues of Cathode Materials for Li-Ion Batteries. *Inorganics* **2014**, *2* (1), 132-154.
52. Wu, F.; Yushin, G., Conversion cathodes for rechargeable lithium and lithium-ion batteries. *Energy & Environmental Science* **2017**, *10* (2), 435-459.

53. Aravindan, V.; Lee, Y.-S.; Madhavi, S., Research Progress on Negative Electrodes for Practical Li-Ion Batteries: Beyond Carbonaceous Anodes. *Advanced Energy Materials* **2015**, 5 (13), 1402225.
54. Cao, F. F.; Deng, J. W.; Xin, S.; Ji, H. X.; Schmidt, O. G.; Wan, L. J.; Guo, Y. G., Cu-Si nanocable arrays as high-rate anode materials for lithium-ion batteries. *Adv Mater* **2011**, 23 (38), 4415-20.
55. Chan, C. K., Patel, R. N., O'connell, M. J., Korgel, B. A., & Cui, Y. , Solution-Grown Silicon Nanowires for lithium ion battery anodes. *ACS Nano* **2010**, 4 (3), 1443-1450.
56. Wu, H.; Chan, G.; Choi, J. W.; Ryu, I.; Yao, Y.; McDowell, M. T.; Lee, S. W.; Jackson, A.; Yang, Y.; Hu, L.; Cui, Y., Stable cycling of double-walled silicon nanotube battery anodes through solid-electrolyte interphase control. *Nat Nanotechnol* **2012**, 7 (5), 310-315.
57. Grimaud, A., Batteries: Beyond intercalation and conversion. *Nature Energy* **2017**, 2 (2).
58. Nookala, M., Kumar, B. and Rodrigues, S., Ionic conductivity and ambient temperature Li electrode reaction in composite polymer electrolytes containing nanosize alumina. *Journal of power sources* **2002**, 111 (1), 165 - 172.
59. Munar, A.; Andrio, A.; Iserte, R.; Compañ, V., Ionic conductivity and diffusion coefficients of lithium salt polymer electrolytes measured with dielectric spectroscopy. *Journal of Non-Crystalline Solids* **2011**, 357 (16-17), 3064-3069.
60. Liu, W.; Liu, N.; Sun, J.; Hsu, P. C.; Li, Y.; Lee, H. W.; Cui, Y., Ionic conductivity enhancement of polymer electrolytes with ceramic nanowire fillers. *Nano Lett* **2015**, 15 (4), 2740-2745.
61. Corporation, N., Measurement principles & methods of Resistance. *Napson Corporation* **2015**, 1 (1), 1-19.
62. Yoon, S. B.; Jegal, J. P.; Roh, K. C.; Kim, K. B., Electrochemical Impedance Spectroscopic Investigation of Sodium Ion Diffusion in MnO₂ Using a Constant Phase Element Active in Desired Frequency Ranges. *Journal of the Electrochemical Society* **2014**, 161 (4), H207-H213.

63. Bandarenka, A. S., Exploring the interfaces between metal electrodes and aqueous electrolytes with electrochemical impedance spectroscopy. *Analyst* **2013**, *138* (19), 5540-5554.
64. Ogihara, N.; Itou, Y.; Sasaki, T.; Takeuchi, Y., Impedance Spectroscopy Characterization of Porous Electrodes under Different Electrode Thickness Using a Symmetric Cell for High-Performance Lithium-Ion Batteries. *The Journal of Physical Chemistry C* **2015**, *119* (9), 4612-4619.
65. Yamada, Y.; Iriyama, Y.; Abe, T.; Ogumi, Z., Kinetics of lithium ion transfer at the interface between graphite and liquid electrolytes: effects of solvent and surface film. *Langmuir* **2009**, *25* (21), 12766-70.
66. Bard, A. J., Faulkner, L. R., Leddy, J., & Zoski, C. G. , *Electrochemical methods: fundamentals and applications*. wiley: New York, 1980; Vol. 2.
67. Wang, M.; Zhao, F.; Guo, Z.; Dong, S., Poly(vinylidene fluoride-hexafluoropropylene)/organo-montmorillonite clays nanocomposite lithium polymer electrolytes. *Electrochimica Acta* **2004**, *49* (21), 3595-3602.
68. Wang, D., Choi, D., Li, J., Yang, Z., Nie, Z., Kou, R., Hu, D., Wang, C., Saraf, L.V., Zhang, J. and Aksay, I.A., Self-assembled TiO₂-graphene hybrid nanostructures for enhanced Li-ion insertion. *ACS Nano* **2009**, *3* (4), 907-914.
69. Guo, P.; Song, H.; Chen, X., Electrochemical performance of graphene nanosheets as anode material for lithium-ion batteries. *Electrochemistry Communications* **2009**, *11* (6), 1320-1324.
70. Guoping, W.; Qingtang, Z.; Zuolong, Y.; Meizheng, Q., The effect of different kinds of nano-carbon conductive additives in lithium ion batteries on the resistance and electrochemical behavior of the LiCoO₂ composite cathodes. *Solid State Ionics* **2008**, *179* (7-8), 263-268.
71. Liu, X.-M.; Huang, Z. d.; Oh, S. w.; Zhang, B.; Ma, P.-C.; Yuen, M. M. F.; Kim, J.-K., Carbon nanotube (CNT)-based composites as electrode material for rechargeable Li-ion batteries: A review. *Composites Science and Technology* **2012**, *72* (2), 121-144.
72. Nitta, N.; Wu, F.; Lee, J. T.; Yushin, G., Li-ion battery materials: present and future. *Materials Today* **2015**, *18* (5), 252-264.

73. Chou, S.-L.; Wang, J.-Z.; Liu, H.-K.; Dou, S.-X., Rapid Synthesis of Li₄Ti₅O₁₂ Microspheres as Anode Materials and Its Binder Effect for Lithium-Ion Battery. *The Journal of Physical Chemistry C* **2011**, *115* (32), 16220-16227.
74. Gaines, L., & Nelson, P., Lithium-Ion Batteries - Possible Materials Issues *13th international battery materials recycling seminar and exhibit, Broward County Convention Center, Fort Lauderdale, Florida* **2009**, 16.
75. Delacourt, C., A. Kwong, X. Liu, R. Qiao, W. L. Yang, P. Lu, S. J. Harris, and V. Srinivasan., Effect of Manganese Contamination on the Solid-Electrolyte-Interphase Properties in Li-Ion Batteries. *Journal of The Electrochemical Society* **2013**, *160* (8), A1099-1107.
76. Belharouak, I.; Koenig, G. M.; Tan, T.; Yumoto, H.; Ota, N.; Amine, K., Performance Degradation and Gassing of Li₄Ti₅O₁₂/LiMn₂O₄ Lithium-Ion Cells. *Journal of the Electrochemical Society* **2012**, *159* (8), A1165-A1170.
77. Vetter, J.; Novák, P.; Wagner, M. R.; Veit, C.; Möller, K. C.; Besenhard, J. O.; Winter, M.; Wohlfahrt-Mehrens, M.; Vogler, C.; Hammouche, A., Ageing mechanisms in lithium-ion batteries. *Journal of Power Sources* **2005**, *147* (1-2), 269-281.
78. Arora, P., White, R.E. and Doyle, M., Capacity Fade Mechanisms and Side Reactions in lithium ion batteries. *Journal of the Electrochemical Society* **1998**, *145* (10), 3647-3667.
79. Lv, J.; Yin, X.; Zeng, Q.; Dong, W.; Liu, H.; Zhu, L., Preparation of carboxymethyl chitosan nanofibers through electrospinning the ball-milled nanopowders with poly (lactic acid) and the blood compatibility of the electrospun NCMC/PLA mats. *Journal of Polymer Research* **2017**, *24* (4).
80. Kiss, E.; Bertoti, I.; Vargha-Butler, E. I., XPS and wettability characterization of modified poly(lactic acid) and poly(lactic/glycolic acid) films. *J Colloid Interface Sci* **2002**, *245* (1), 91-8.
81. Shakesheff, K. M., Evora, C., Soriano, I. and Langer, R., The adsorption of poly (vinyl alcohol) to biodegradable microparticles studied by X-ray photoelectron spectroscopy (XPS). *Journal of colloid and interface science* **1997**, *185* (2), 538-547.

82. He, W.; Cui, Z.; Liu, X.; Cui, Y.; Chai, J.; Zhou, X.; Liu, Z.; Cui, G., Carbonate-linked poly(ethylene oxide) polymer electrolytes towards high performance solid state lithium batteries. *Electrochimica Acta* **2017**, *225*, 151-159.
83. He, Y.-B.; Liu, M.; Huang, Z.-D.; Zhang, B.; Yu, Y.; Li, B.; Kang, F.; Kim, J.-K., Effect of solid electrolyte interface (SEI) film on cyclic performance of Li₄Ti₅O₁₂ anodes for Li ion batteries. *Journal of Power Sources* **2013**, *239*, 269-276.
84. Verma, P.; Maire, P.; Novák, P., A review of the features and analyses of the solid electrolyte interphase in Li-ion batteries. *Electrochimica Acta* **2010**, *55* (22), 6332-6341.
85. Kim, M. J.; Flowers, P. F.; Stewart, I. E.; Ye, S.; Baek, S.; Kim, J. J.; Wiley, B. J., Ethylenediamine Promotes Cu Nanowire Growth by Inhibiting Oxidation of Cu(111). *J Am Chem Soc* **2017**, *139* (1), 277-284.
86. Park, S., & Jayaraman, S., Enhancing the quality of life through wearable technology. *IEEE Engineering in medicine and biology magazine* **2003**, *22* (3), 41-48.
87. Qin, T.; Peng, S.; Hao, J.; Wen, Y.; Wang, Z.; Wang, X.; He, D.; Zhang, J.; Hou, J.; Cao, G., Flexible and Wearable All-Solid-State Supercapacitors with Ultrahigh Energy Density Based on a Carbon Fiber Fabric Electrode. *Advanced Energy Materials* **2017**, 1700409.
88. Stoppa, M.; Chiolerio, A., Wearable electronics and smart textiles: a critical review. *Sensors (Basel)* **2014**, *14* (7), 11957-92.
89. Du, Z.; Rollag, K. M.; Li, J.; An, S. J.; Wood, M.; Sheng, Y.; Mukherjee, P. P.; Daniel, C.; Wood, D. L., Enabling aqueous processing for crack-free thick electrodes. *Journal of Power Sources* **2017**, *354*, 200-206.
90. Bitsch, B.; Dittmann, J.; Schmitt, M.; Scharfer, P.; Schabel, W.; Willenbacher, N., A novel slurry concept for the fabrication of lithium-ion battery electrodes with beneficial properties. *Journal of Power Sources* **2014**, *265*, 81-90.
91. Jeschull, F.; Brandell, D.; Edstrom, K.; Lacey, M. J., A stable graphite negative electrode for the lithium-sulfur battery. *Chem Commun (Camb)* **2015**, *51* (96), 17100-3.

92. Liu, D.; Chen, L.-C.; Liu, T.-J.; Fan, T.; Tsou, E.-Y.; Tiu, C., An Effective Mixing for Lithium Ion Battery Slurries. *Advances in Chemical Engineering and Science* **2014**, *04* (04), 515-528.
93. Zhang, R.; Yang, X.; Zhang, D.; Qiu, H.; Fu, Q.; Na, H.; Guo, Z.; Du, F.; Chen, G.; Wei, Y., Water soluble styrene butadiene rubber and sodium carboxyl methyl cellulose binder for ZnFe₂O₄ anode electrodes in lithium ion batteries. *Journal of Power Sources* **2015**, *285*, 227-234.
94. Cruz, M. A.; Ye, S.; Kim, M. J.; Reyes, C.; Yang, F.; Flowers, P. F.; Wiley, B. J., Multigram Synthesis of Cu-Ag Core-Shell Nanowires Enables the Production of a Highly Conductive Polymer Filament for 3D Printing Electronics. *Particle & Particle Systems Characterization* **2018**, *35* (5), 1700385.
95. Stewart, I. E.; Ye, S.; Chen, Z.; Flowers, P. F.; Wiley, B. J., Synthesis of Cu-Ag, Cu-Au, and Cu-Pt Core-Shell Nanowires and Their Use in Transparent Conducting Films. *Chemistry of Materials* **2015**, *27* (22), 7788-7794.
96. Aguiló-Aguayo, N.; Espiñeira, P. P.; Manian, A. P.; Bechtold, T., Three-dimensional embroidered current collectors for ultra-thick electrodes in batteries. *RSC Adv.* **2016**, *6* (74), 69685-69690.
97. Rana, K.; Kim, S. D.; Ahn, J. H., Additive-free thick graphene film as an anode material for flexible lithium-ion batteries. *Nanoscale* **2015**, *7* (16), 7065-71.
98. Shen, F.; Luo, W.; Dai, J.; Yao, Y.; Zhu, M.; Hitz, E.; Tang, Y.; Chen, Y.; Sprenkle, V. L.; Li, X.; Hu, L., Ultra-Thick, Low-Tortuosity, and Mesoporous Wood Carbon Anode for High-Performance Sodium-Ion Batteries. *Advanced Energy Materials* **2016**, *6* (14), 1600377.
99. Chan, C. K.; Peng, H.; Liu, G.; McIlwrath, K.; Zhang, X. F.; Huggins, R. A.; Cui, Y., High-performance lithium battery anodes using silicon nanowires. *Nat Nanotechnol* **2008**, *3* (1), 31-5.
100. Tang, Y.; Zhang, Y.; Li, W.; Ma, B.; Chen, X., Rational material design for ultrafast rechargeable lithium-ion batteries. *Chem Soc Rev* **2015**, *44* (17), 5926-40.

Biography

Christopher Reyes was born August 8th, 1985 in Corpus Christi, TX. He is a first-generation college student who is the first in entire his family to receive undergraduate degree and the first to pursue an advanced degree. He graduated from Texas State University in San Marcos, TX in 2014 with a B.S. in Applied Mathematics and a minor in Chemistry. He began his PhD program in Chemistry at Duke University in August 2014 under the supervision of Dr. Benjamin J Wiley. His research consisted of the acoustic manipulation of nanoparticles, 3D printing of lithium ion batteries and utilizing conductive nanomaterials in lithium ion graphite anodes. He has authored two first author publications; The Limits of Primary Radiation Forces in Bulk Acoustic Standing Waves for Concentrating Nanoparticles, A Complete Lithium Ion Battery Fabricated Using Fused Filament Fabrication, and has coauthored 6 publication; Stretchable Conductive Composites from CuAg Nanowire Felt, Multigram Synthesis of Cu-Ag Core-Shell Nanowires Enables the Production of a Highly Conductive Polymer Filament for 3D Printing Electronics, 3D Printing Electronic Components and Circuits with Conductive Thermoplastic Filament, Microwave Metamaterials made by fused deposition 3D printing of a highly conductive copper-based filament, Assembly of Colloidal Molecules, Polymers, and Crystals in Acoustic and Magnetic Fields and Facile Hydroxylation of Halloysite Nanotubes for Epoxy Nanocomposite Applications. He was a National Science

Foundation Graduate Research Fellow, Materials Research Science and Education Center
Fellow and a Department of Education GAAAN Fellow.